Powder Technology 331 (2018) 74–97

Contents lists available at ScienceDirect

Powder Technology

journal homepage: www.elsevier.com/locate/powtec

Review

A review of powdered additive manufacturing techniques for Ti-6al-4v biomedical applications

W.S.W. Harun [a,*], N.S. Manam [a], M.S.I.N. Kamariah [a], S. Sharif [b], A.H. Zulkifly [c], I. Ahmad [d], H. Miura [e]

[a] Green Research for Advanced Materials Laboratory (GramsLab), Faculty of Mechanical Engineering, Universiti Malaysia Pahang, 26600 Pekan, Pahang, Malaysia
[b] Department of Materials, Manufacturing & Industrial Engineering, Faculty of Mechanical Engineering, Universiti Teknologi Malaysia, 81310 Skudai, Johor, Malaysia
[c] Kulliyah of Medicine, International Islamic University Malaysia, Kuantan Campus, Pahang, Malaysia
[d] Additive Manufacturing Research and Innovation Centre (AMRIC), Kolej Kemahiran Tinggi MARA Kuantan, 25150 Kuantan, Pahang, Malaysia
[e] Research Center for Steel in Kyushu University, Kyushu University, 744 Motooka, Nishi-ku, Fukuoka 819-0395, Japan

ARTICLE INFO

Article history:
Received 23 November 2017
Received in revised form 28 February 2018
Accepted 7 March 2018
Available online 10 March 2018

Keywords:
Additive manufacturing process
Metal-additive manufacturing
Ti-6Al-4V
Microstructure
Powder metallurgy

ABSTRACT

Rapid advancements in science and technology have assured biomaterials and their associated fields towards becoming a multimillion-dollar industry. Biomaterials have been shown as one of the most promising materials for biomedical implant development. As such, this article intends to provide a comprehensive review of metal additive manufacturing (metal-AM) processes evolution used in biomedical applications. The most common types of metal-AM methods practised today are Selective Laser Sintering (SLS), Selective Laser Melting (SLM), Direct Metal Laser Sintering (DMLS), Electron Beam Melting (EBM) and Laser Engineered Net Shaping (LENS). The present review also covers the application of these metal-AM systems in Ti-6Al-4V-based implants fabrication. The scientific challenges and critical issues towards improving the biomaterial properties so that they are more notable in the biomedical industry are also discussed.

Contents

1. Introduction to metal additive manufacturing (metal-AM)

Today most biomedical implants [1–7] are produced from austenitic stainless steel [8–28], cobalt-chromium-based alloys [29–31], and titanium with its alloys [32–83]. These implants are preferably fabricated by using advanced manufacturing techniques, such as metal additive manufacturing (metal-AM) technologies for customised properties [84–96]. Typical examples of advanced metal-AM technologies are Selective Laser Sintering (SLS) [97], Selective Laser Melting (SLM) [98–109], Direct Laser Melting Sintering (DMLS) [110–112], Electron Beam Melting (EBM) [113–121] and Laser Engineered Net Shaping (LENS) [122,123].

* Corresponding author.
E-mail address: sharuzi@ump.edu.my (W.S.W. Harun).

https://doi.org/10.1016/j.powtec.2018.03.010
0032-5910/

A process known as Powder Bed Fusion (PBF) laser sintering was patented and copyrighted as a selective laser sintering or SLS technique [124,125]. In the early 1990s, 3 Dimensional (3D) printed components produced by SLS technique were limited to metal alloy powders, such as tin, copper, and Pb–Sn solder [126,127]. The metal-AM technique was initially licensed to Electro Optical Systems Gesellschaft mit beschrankter Haftung (EOS GmbH). However, now many different manufacturers have commenced the manufacturing of powder-bed equipment for the metal generation, for instance, Concept Laser, SLM Solutions, 3D Systems, and Renishaw. Also, soon after the SLS technique was patented, researchers from Massachusetts Institute of Technology (MIT) patented a procedure called '3D printing', which exploits the inkjet printing mechanism to deposit the binder [128,129]. Contrary to SLS technique, Direct Energy Deposition (DED) is another class of method which completely melts rather than partially melts the powder particles [130]. Principally, DED technique adopts the welding technologies mechanism. Since the DED technique was agonised with several technological problems, Sandia National Research Lab had proposed a new approach to overcome the problem by integrating a laser heat source into the DED system [131]. The innovation was popularised and trademarked as Laser Engineered Net Shaping (LENS), which is a subset of DED [132]. Meanwhile, sheet lamination is a technique under the metal-AM group that utilises ultrasonic welding and Computer Numerical Control (CNC) milling to weld together a stack of sheets to fabricate 3D components. This method was introduced and popularised by Dawn White of Solidica, Inc. in 1999 [133,134]. Besides, in 2000, an investigation in Sweden had prompted another new powder-bed method called Electron Beam Melting (EBM) which uses an electron beam to melt the powder particles [135,136]. The innovation of additive manufacturing process was rising until Desktop Metal technology was invented in 2015 which involved a number of material scientists and other engineers from MIT [137]. The history of metal-AM evolution is briefly explained in Table 1 [138–140]. Meanwhile,Table 2 lists the differences among commonly used metal-AM methodologies [132,141–143].

Metallic components manufactured via metal-AM techniques are known to have numerous advantages and practical applications [144]. The ability to adapt the component strength has further encouraged them for various applications. However, the major disadvantage of biomedical implants prepared by metal-AM techniques is the microstructure produced which limits the mechanical performance of the produced components [145,146]. Porous biomaterials produced via this method have three main advantages as compared to those produced by conventional manufacturing technologies. They are 1) porous biomaterial quality has a degree of controllability, which is useful in the design standpoint,specifically the mechanical properties as they are extremely dependent on the formed microstructure [145]. Therefore, a designer, by implication, could vary the mechanical properties of porous biomaterials by simply altering the orientation of the microstructure. 2) The feasibility of having different microstructures within a particular texture of porous materials, or by combining solid materials with porous materials. Since each designated microstructure offers different mechanical properties, a region within the implant can be optimised to reduce stress shielding [147], and finally 3) construction of patient-specific implants based on specific requirements.

This paper is aimed to provide a comprehensive review the mechanisms and applications of five metal-AM methods (SLS, DMLS, SLM, EBM, and LENS) in Ti-6Al-4V alloy powder processing. The fabrication processes and the microstructural evolution of Ti-6Al-4V alloy for each approach are also discussed.

2. Ti-6Al-4V by using Selective Laser Sintering (SLS)

The SLS technique focusses on highly-dense components production through the combination of post-processing techniques [148–150], particularly in the fabrication of biocompatible polymers for porous tissue engineering scaffolds [151,152]. The manufacture of biomedical implants with a porous structure that imitates the mechanical properties of the bone is an interesting issues in biomedical application especially for orthopedic. Since polymeric powders are the core materials that are built using SLS technique, very limited study is currently available on the use of Ti-6Al-4V powders. The SLS technique allocates the manufacture of complex shapes using 3D model, which present the vision of organizing porous biometallic implants, where porosity and stiffness can be correctly used to the need of human being.

2.1. Microstructure of Ti-6Al-4V by SLS

The intention of study prepared by J. Maszybrocka et al. [153] is to examine the microstructure of porous Ti-6Al-4V manufactured using SLS technique. The microstructure created the qualitative assessment of the 3D shape of a presented surface. Fig. 1 illustrated the examination of the struts surface under Scanning Electron Microscopy (SEM). They demonstrated their complex microstructure of porous Ti-6Al-4V powders or moderately melted agglomerates were attached to the surface. The existence of attached particles was the result of the technique for generating the porous structures [154,155]. The big differences in temperature among the nearby loose powder and sintered material encouraged the thermal diffusion incident which consequences in incomplete melting of powder and the attachment to the struts. The powder component can be melted by the laser beam carried on the surface of the powder as formerly noticeable path and subsequently attached to

Table 1
History of metal-AM development.

Year	Description	References
1984	• Works to build 3D parts from powder begins by Deckard and Beaman using a 100 W YAG laser heat source	[138]
1986	• Betsy initiated before continuing with SLS study by Deckard and Beaman • University of Texas owns the SLS patent by Deckard	[138]
1989	• Patent for inkjet binder deposition or '3D Printing' has granted at MIT by Sachs and Cima	[129]
1990	• Manriquez Frayre and Bourell has made the first 3D printed metal part by SLS	[128,129]
1993	• Larson has patented the EBM process	[135]
1995	• EOS launches first commercial DMLS machine (EOSINT M 250) • LENS development has been initiated by Sandia International Laboratories	[131]
1997	• SLS rights have been authorised to EOS by 3D Systems. • EOS focuses on the powder bed fusion technology development	[131]
1999	• Dawn White of Solidica Inc. patented the ultrasonic consolidation technology	[133,134]
2000	• Andersson and Larsson patented EBM process, and Arcam AB receives the license	[136]
2001	• 3D Systems acquires DTM to commercialise SLS technology	[138]
2002	• First commercial machine, the S12 launches by Arcam	[131]
2007	• EBM begins to build CE-certified hip implant	[132,138]
2012	• 3D Systems acquires Z-Corp, the patent owner of inkjet binder process	[139]
2015	• Desktop Metal technology was founded	[137,140]

Table 2
Comparisons among metal-AM processes.

Metal AM	Founder	Original corporation	Date of patent	Deposition mode	Process type	Accuracy (mm)	Maximum build size (mm^3)	References
SLS	Carl Deckard and Joe Beaman	University of Texas at Austin	1986	Laser beam	PBF	High, ±0.05	700 × 380 × 560	[143]
DMLS	Hans Langer and Hans Steinbichler	EOS and 3D Systems	1989	Laser beam	PBF	High, ±0.05	350 × 350 × 600	[142]
SLM	Dieter Schwarze and Matthias Fockele	Fraunhofer Institute for Laser Technology (ILT)	1995	Laser beam	PBF	High, ±0.04	280 × 280 × 365	[141]
EBM	Lars-Erik Andersson & Morgan Larsson	Arcam AB	2000	Electron beam	PBF	±0.2	200 × 200 × 180	[132]
LENS	Jeantette et al.	Sandia National Laboratories	1998	Laser beam	DED	X–Y plane ±0.05; Z axis ± 0.38	N/A	[132]

each layer boundary. In case of inclined struts the developed practice it is partially founded on the loose powder and the earlier sintered layer of material. Several metal particles below the layer possibly completely or partly melted and then attached with a lower layer of material. Its clarified struts of lower surfaces had greater roughness than upper surfaces.

Fig. 2 illustrated a 3D images of the struts fragments. The utilisation of the CT scanner permitted for surface morphology assessment of the struts all over the quantity of Ti-6Al-4V porous structure. Identical to the outer layer, the struts within the porous structure remained moderately melted the Ti-6Al-4V powder or agglomerates, which was

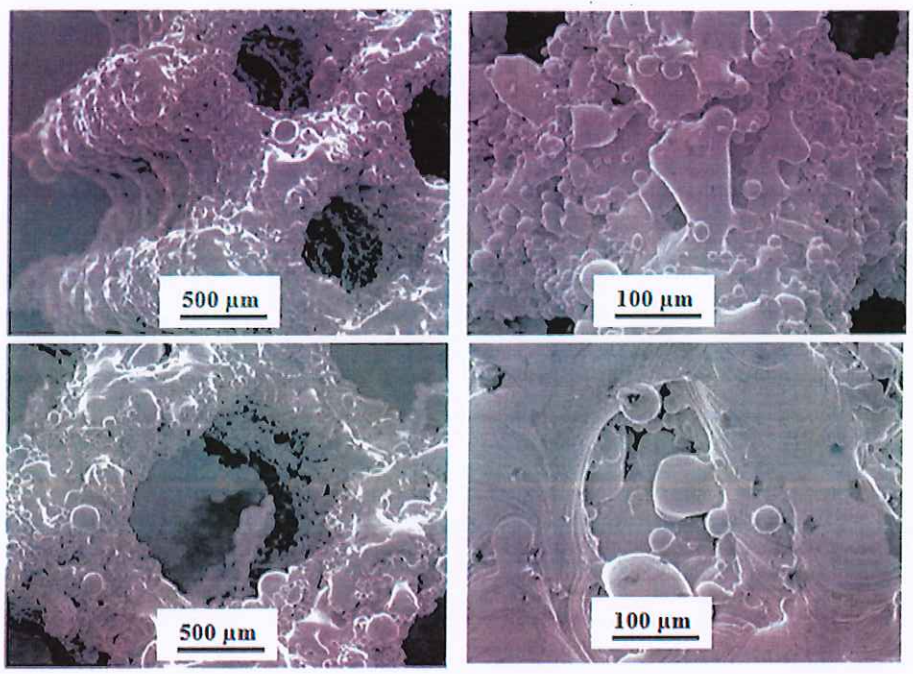

Fig. 1. Struts microstructure of porous Ti-6Al-4V [153].

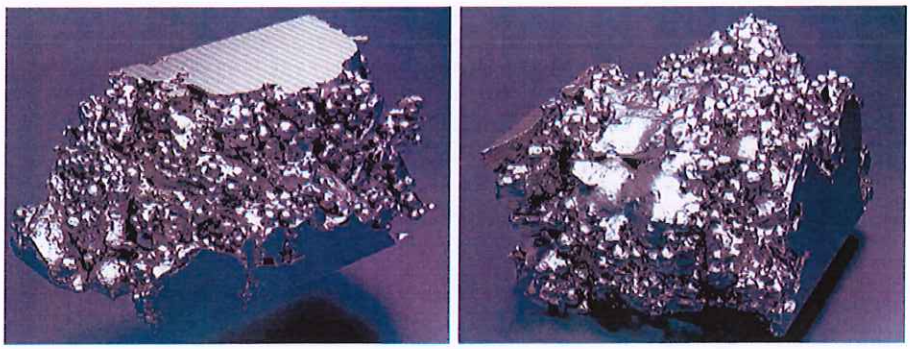

Fig. 2. 3D images of struts fragments by X-ray computer microtomography [153].

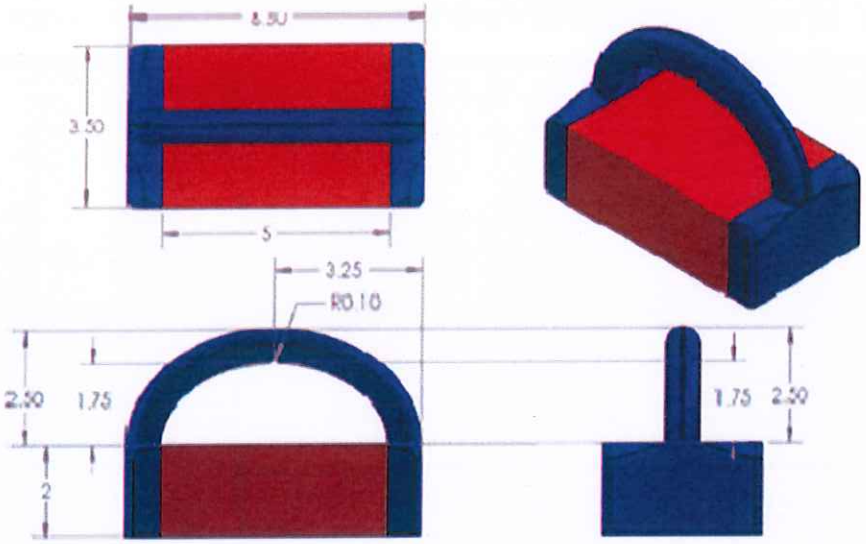

Fig. 3. Mechanical implant design; red signifies solid or trabecular porosity based on the experimental group where as blue signifies the arch and solid side support for mechanical test [156]. (For interpretation of the references to color in this figure legend, the reader is referred to the web version of this article.)

estimated by SEM images in Fig. 1. The studies in [153] proved that the struts of porous Ti-6Al-4V created by SLS technique have a complex surface morphology. The expanded of interfacial area ratio, calculated from the source of microtomography measurements has attained an assessment of up to 180% and 34 μm for the mean square deviation of the surface.

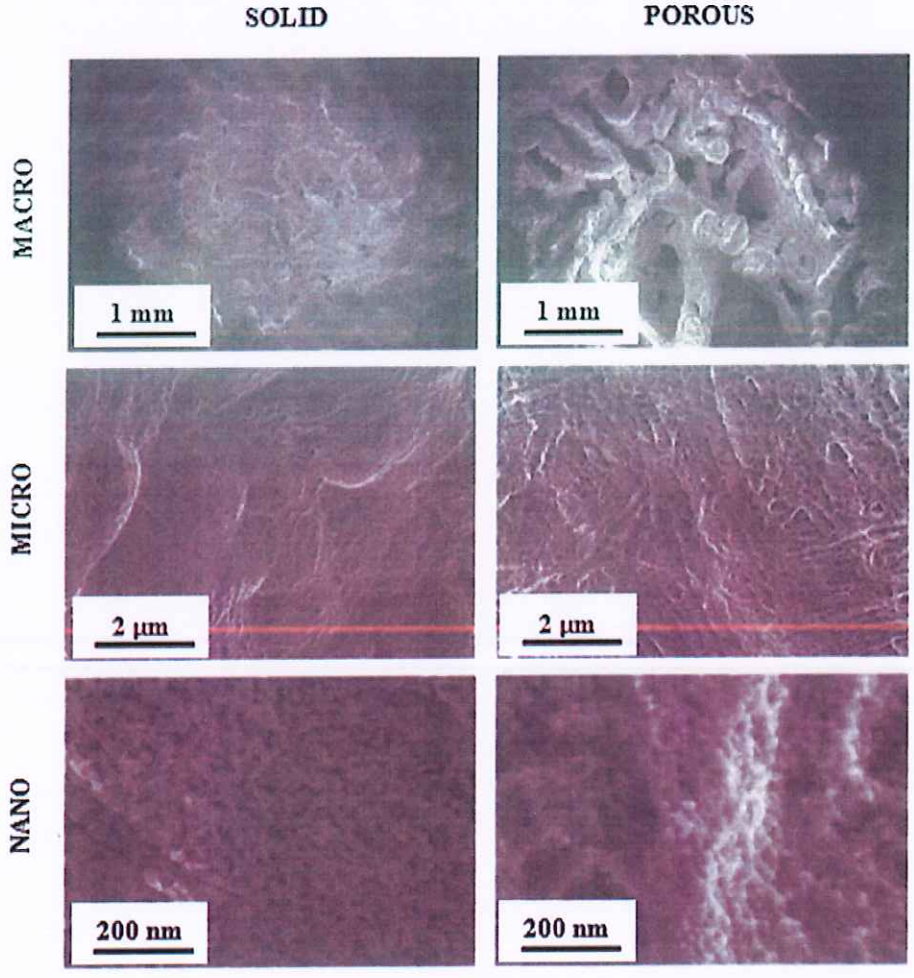

Fig. 4. Image by SEM for solid (left) and 3D porous implants (right) show nano, micro and macro surface topography [156].

Another researcher that has been study about Ti–6Al–4V fabricated by SLS technique was Alice Cheng et al. [156]. They have investigated the capability of 3D implants with micro−/nano-rough surfaces and trabecular-bone-inspired porosity to improve the ingrowth of the vertical bone. By increasing the porosity of the Ti–6Al–4V, the compressive moduli of the builds decreased to enhanced imitate of the natural modulus of bone. The female and male human osteoblasts were seeded on builds to evaluate the cell morphology and reaction. Then, the implants were located on a rat calvaria for 10 weeks to review the ingrowth of vertical bone, included the mechanical strength. The result of porous implants which located in-vivo had an typical of 3.1 ± 0.6 mm^3 vertical bone growth. They also had considerably superior pull-out strength values than the solid implants. Fig. 3 demonstrated the implants for the mechanical test. It had been included an extra arch 2.5 mm in height attached to the solid side supports. Where as, Fig. 4 illustrated the nano, micro, and macro surface topography image by SEM for solid (left) and 3D porous implants (right) after the surface treatment on both solid and porous implants.

Then, they also reported the values of pull-out strength of implants, which were notably higher for porous and porous+ human demineralized bone matrix putty (DBX) compared to solid implants. In the study, the researchers indicated that the employ of DBX did not give an important increase in pull-out force for porous implants which showed in Fig. 5a. The optical image in Fig. 5(b) and SEM image in

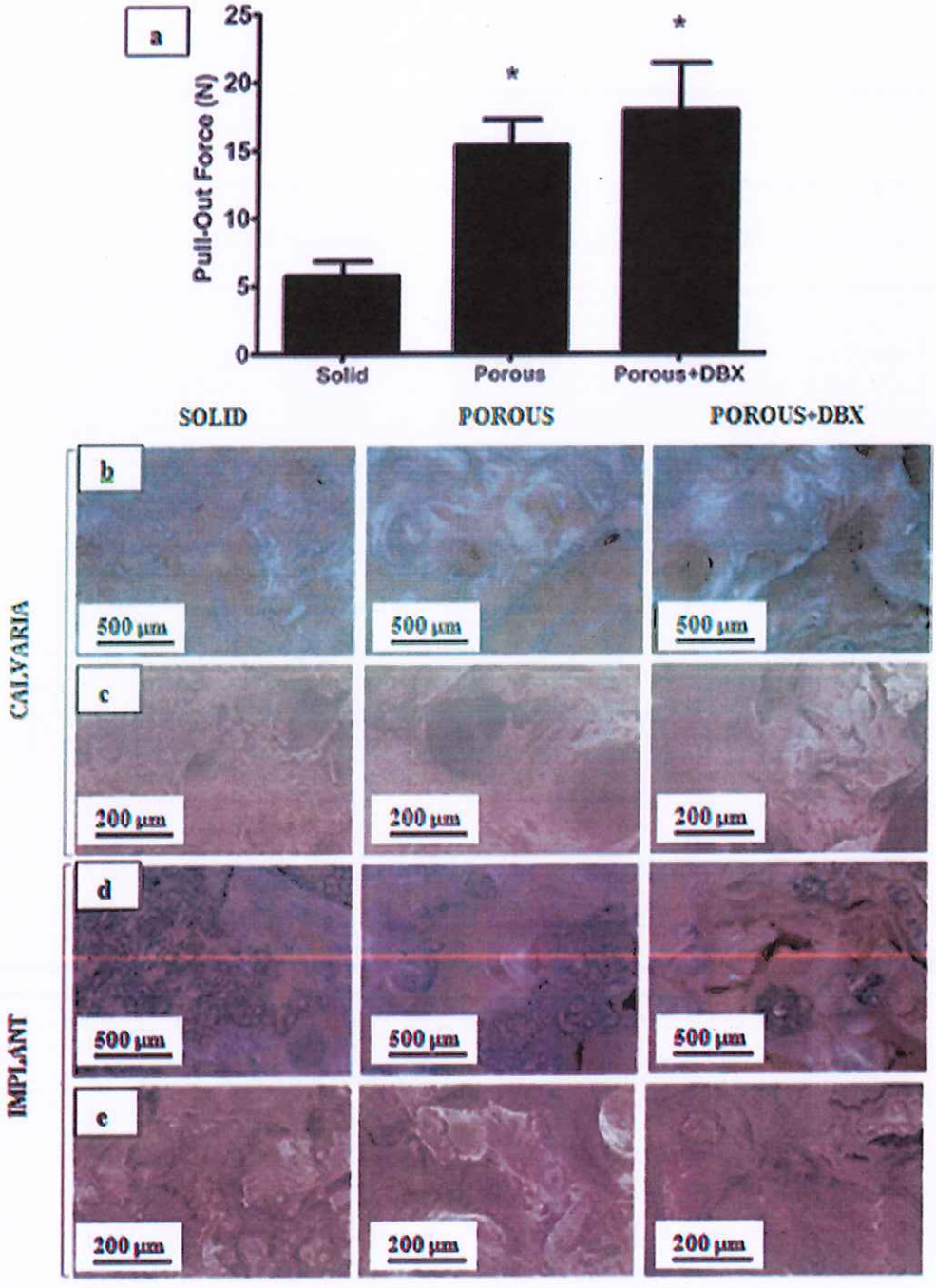

Fig. 5. Pull-out force after 10 weeks implantation (a), under OM (b, d) and SEM (b, e) for calvaria (b, c) and implant (d, e) after the mechanical test [156].

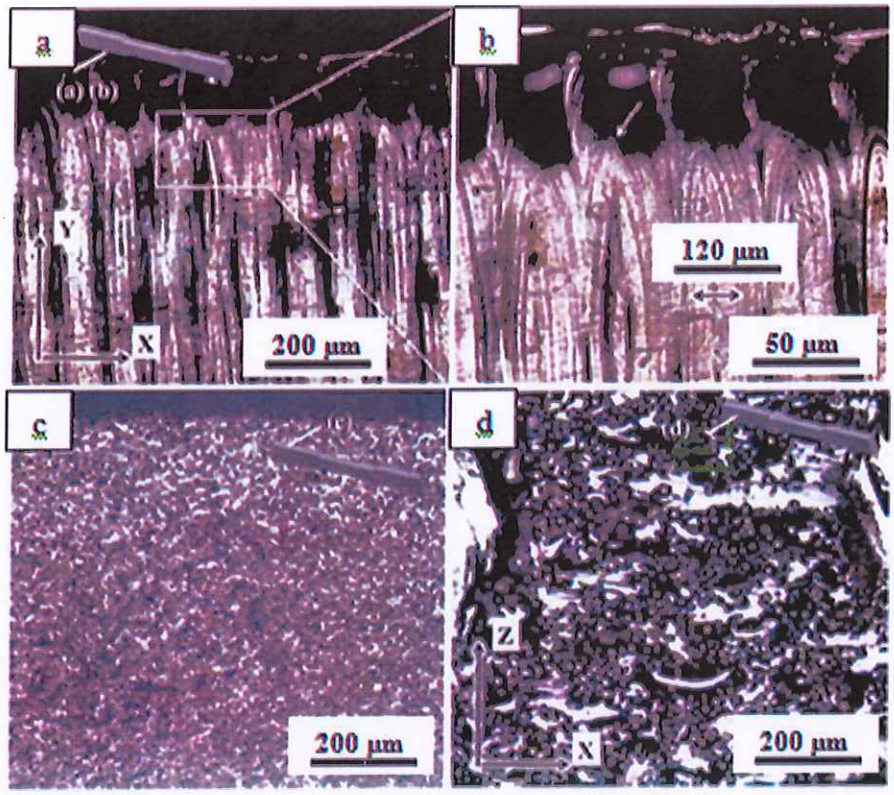

Fig. 6. Microstructure of the DMLS Ti-6Al-4V specimen: (a) bottom deposition plane (XY plane), (b) the remaining scan pattern on the surface, (c) top deposition plane (XY plane), and (d) building plane (XZ plane) [171].

Fig. 5(c) of rat calvaria after the mechanical test illustrated a comparatively smooth surface for calvaria with solid implants. Where as, the calvaria with porous implants demonstrated rough surfaces of bone growth and breaking points through the testing. Fig. 5(d) and (e) which shows optical and SEM images of implants after the mechanical test, respectively, reported an inadequate periosteum and bone on solid implants. Mean while, inside pores of porous implants showed large sections of bone and periosteum were included.

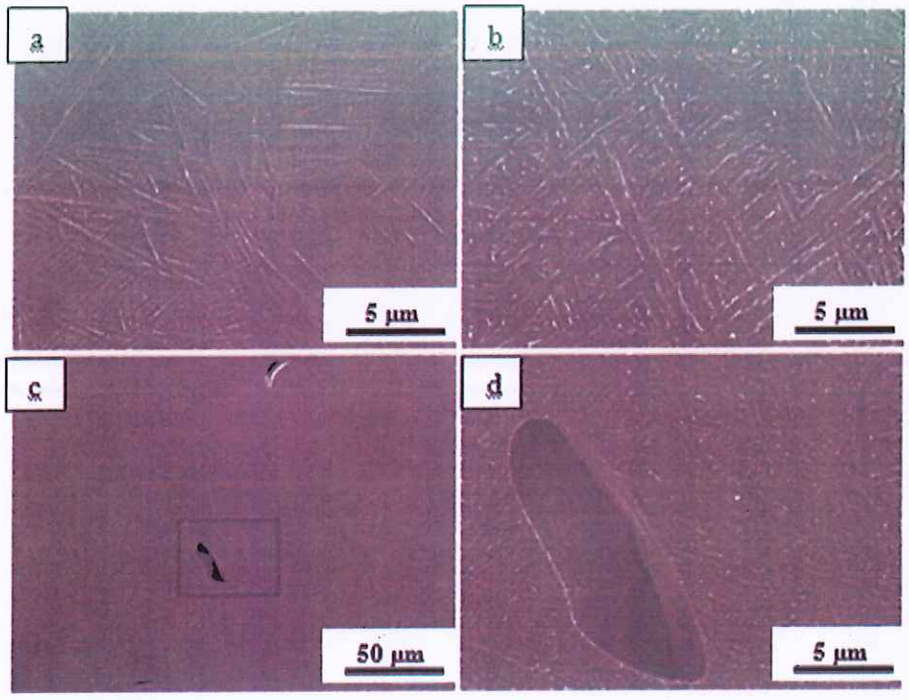

Fig. 7. SEM images of: (a) DMLS, (b) 799 °C heat-treated, (c) microstructure of the surface pores of Ti-6Al-4V specimens, and (d) image of highlighted area in (c) [171].

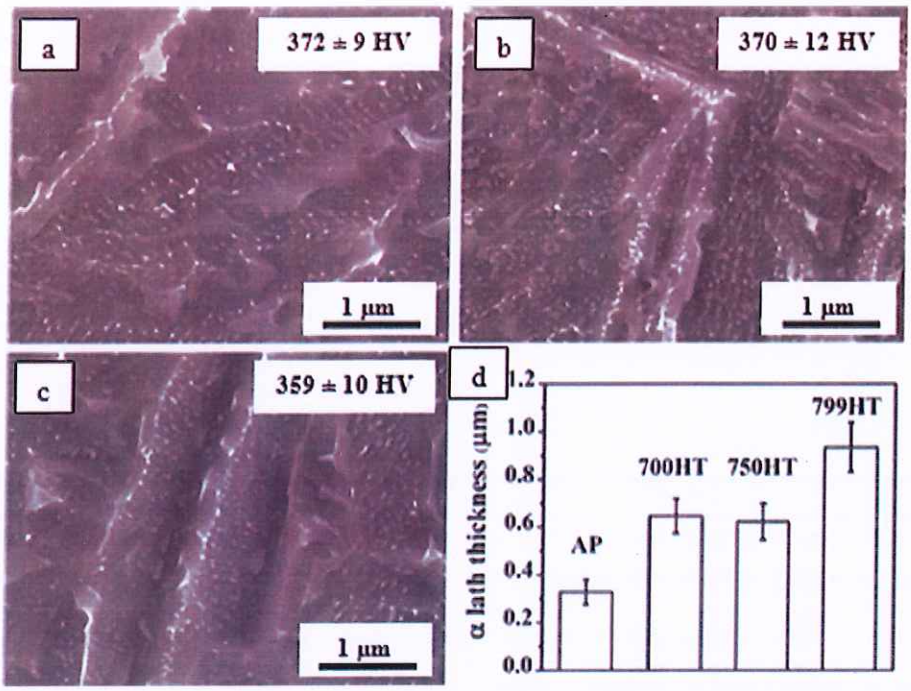

Fig. 8. Microstructure of DMLS post-annealed Ti-6Al-4V specimens at temperatures of: (a) 700, (b) 750, and (c) 799 °C with specified Vickers hardness, (d) Average thickness of α lath with standard deviation of DMLS and post-annealed Ti-6Al-4V specimens [171].

In conclusion, Alice Cheng et al. specified that the ingrowth of new bone into the pores of the implant was highly connected with the mechanical strength of the boundary. The pull-out force values, demonstrating better osseointegration for porous Ti–6Al–4V implant manufactured by SLS technique contrast to solid implants, despite of DBX application. It was distinguished that both solid and porous Ti–6Al–4V implants in this study had nanoscale and microscale surfaces, which has been revealed previously to increase the osteogenic differentiation of osseointegration in vivo and mesenchymal stem cells in vitro [157,158]. Hence, the superior mechanical strength and bone to implant contact renowned with porous implants was an evidence of their better surface area consequential from their porosity, and not because of the variation of the surface processing only.

3. Ti-6Al-4V by using Direct Metal Laser Sintering (DMLS)

The DMLS technique is presently capable of producing close to fully dense specimens (close to 99.7% dense) [159,160]. As reported by many researchers, the DMLS fabricated highly-dense titanium alloys are proven to have mechanical properties that are practically identical to the conventionally manufactured alloys [111,161–168]. Sharon L. Hyzy et al. also suggested that DMLS is the best technique to fabricate Ti-6Al-4V implants as compared to other traditional methods [169]. Whereas, R. Konecna et al. proved that the long fatigue crack growth resistance of Ti-6Al-4V alloys fabricated by using DMLS technique was entirely as good as the traditionally manufactured specimen. Additionally, Sazzad Hossain Ahmed et al. found that the DMLS process parameters, such as laser scanning speed and laser power significantly influenced the formed microstructure and mechanical properties of the fabricated Ti-6Al-4V specimen [170].

3.1. Microstructure of Ti-6Al-4V by using DMLS

Yangzi Xu et al. studied the effects of the post-annealing treatment on the microstructure and mechanical properties of DMLS sintered Ti-6Al-4V alloys at different temperatures (700 °C, 750 °C and 799 °C)

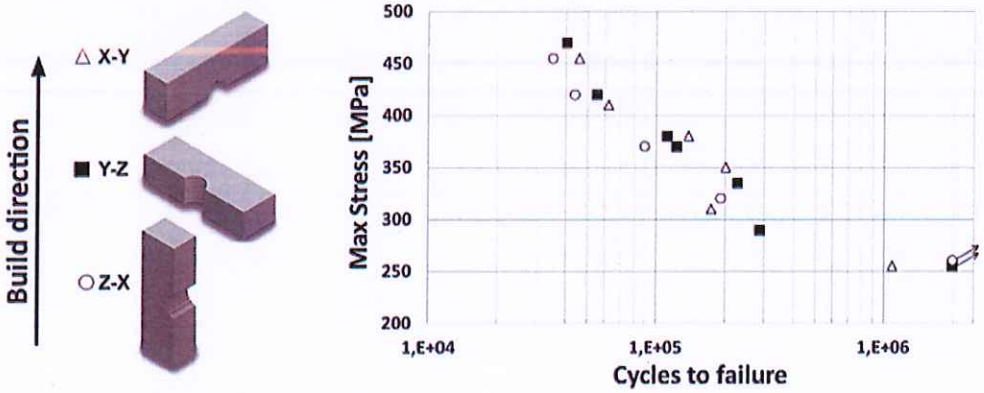

Fig. 9. Fatigue life of DMLS Ti-6Al-4V specimens, $R = 0$ [172].

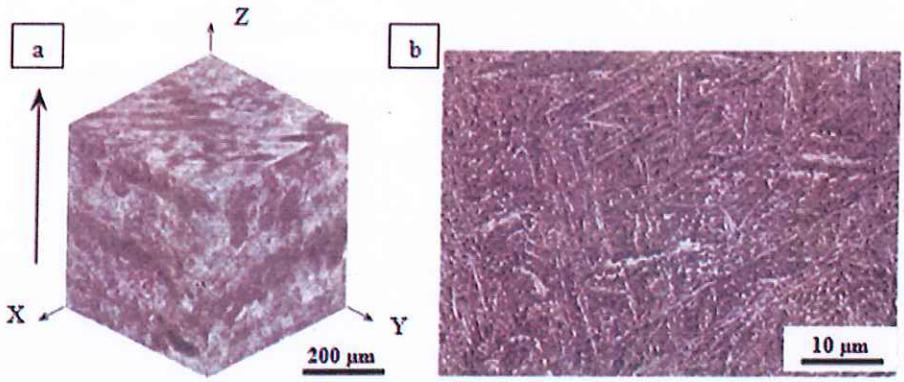

Fig. 10. Microstructure of DMLS Ti-6Al-4 V specimen fabricated at 720 °C and 3 h for stress relief and laser power of 400 W: (a) 3D shape of layered texture, (b) needles of α phase in β matrix [172].

and 4 h of soaking time [171]. Their investigation revealed that the annealing treatment temperature had influenced the microstructure of the sintered alloy. Fig. 6(a) displays the microstructure of the bottom deposition plane (XY plane) of DMLS Ti-6Al-4V specimens with the inset schematically showing the considered plane, meanwhile Fig. 6(b) specifies the remaining scanned pattern of the surface. The white arrow indicates the zigzag scanned pattern, while the double arrows show the distance between two adjacent scanned vectors with a dimension of 1.2×10^{-4} m (120 μm). Whereas, Fig. 6(c) demonstrates the microstructure at the top deposition plane (XY plane). The top plane of the as-printed Ti-6Al-4V specimens was observed to be composed of incompletely sintered particles and lacked the zigzag sintering

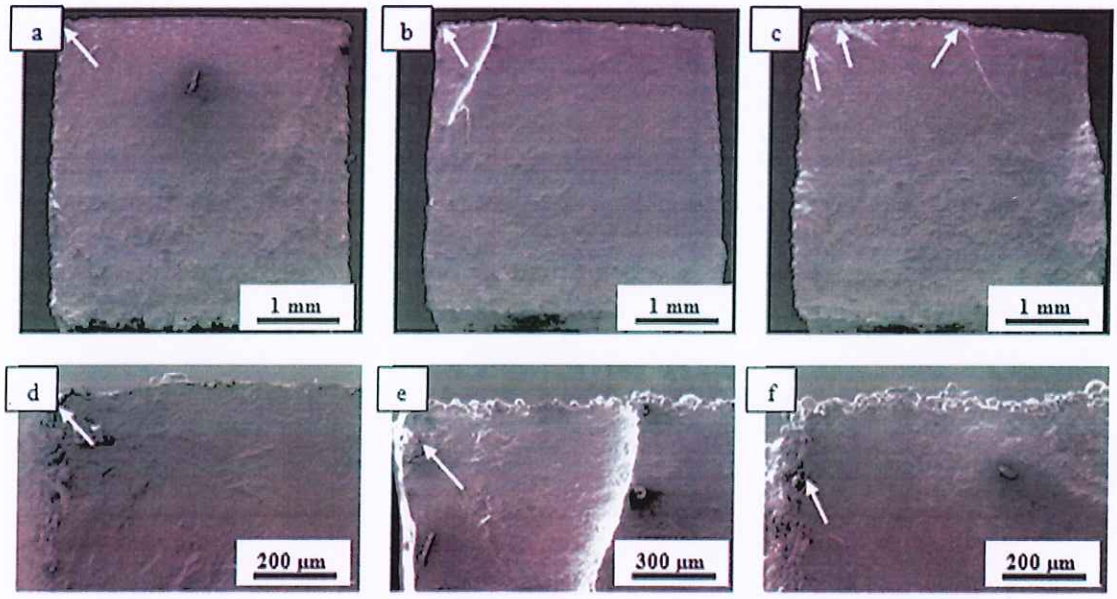

Fig. 11. Locations of crack initiation with regard to the build orientation: (a) X-Y, (b) Y-Z, (c) Z-X fracture surfaces, and (d-f) locations of crack initiation [172].

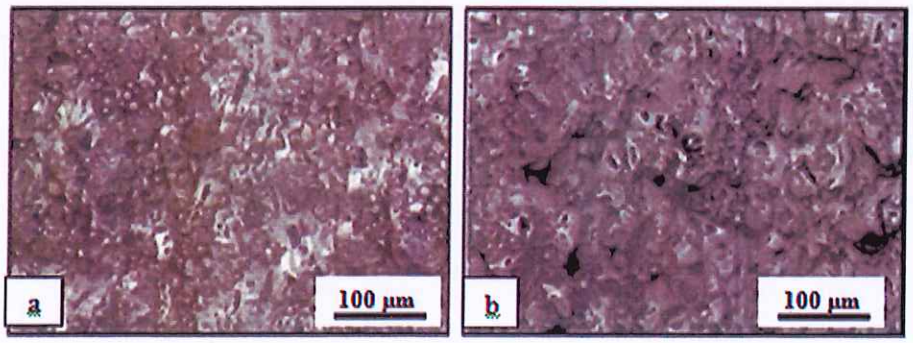

Fig. 12. Horizontally-grown surfaces of DMLS Ti-6Al-4V specimens: (a) as-fabricated and (b) electropolished [175].

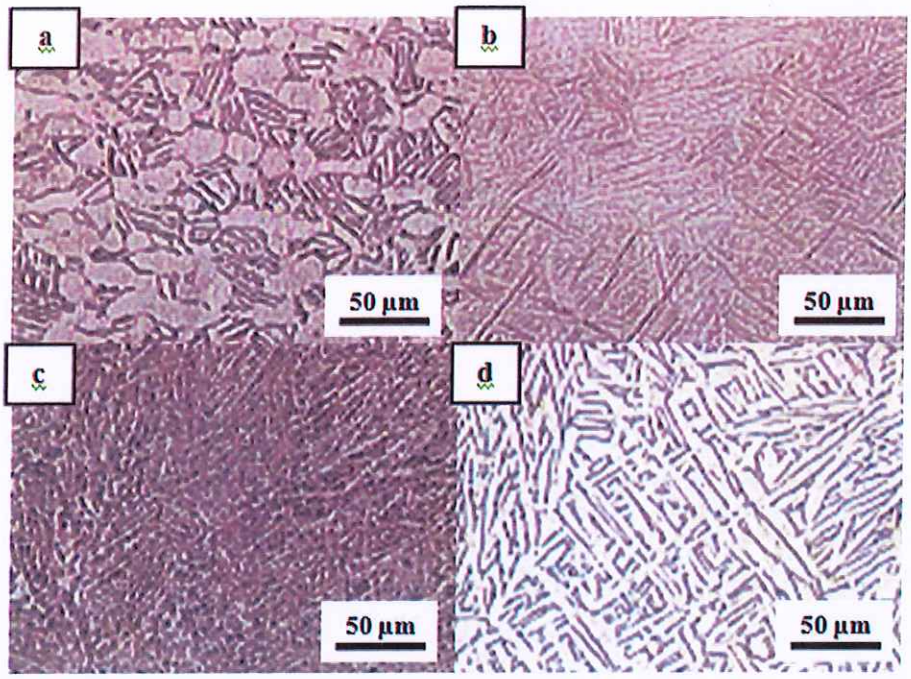

Fig. 13. Microstructures of Ti-6Al-4V specimen: (a) wrought, (b) horizontal DMLS, (c) vertical DMLS, and (d) horizontal DMLS after HIP at 900 °C and 102 MPa [175].

pattern, which contradicted with the image shown in Fig. 6(a). Correspondingly, the image in Fig. 6(d) shows the microstructure at the vertical building plane (XZ plane) whereby, the rough surface observed was testified to be caused by the incomplete sintered powder particles. The different microstructure observed between the building and the deposition planes are believed to be due to the zigzag scanning and layerwise building technique used.

The SEM image in Fig. 7 presents (a) DMLS and (b) 799 °C heat-treated Ti-6Al-4V specimens. The DMLS specimens are described as having an acicular martensitic microstructure which is different from the commercial Grade 5 alloy. Whereas, the image in Fig. 7(c) shows an elongated shape of surface pores after the heat-treatment of Ti-6Al-4V specimens. From the image analysis, the porosity of DMLS and 799 °C heat-treated Ti-6Al-4V specimens were reported to be 0.29 and 0.074%, respectively. The highlighted area in Fig. 7(d) shows the microstructure of lower solid layer along the edge of the elongated pores. Despite the microstructural change in the as-printed specimen, the other concern of laser processing is the porosity formation. Even though the DMLS specimens frequently possess elongated and spherical pores due to insufficient sintering and entrapped gas [114], the process of post-annealing treatment can be executed to improve the amount of porosity. A study conducted by Xu, Y. et al. [171] showed that the post-annealing treatment could reduce the porosity in printed specimens within the range of 0.29 to 0.74%, however, the remaining pores were still expected to influence the mechanical properties. Thus, the HIP process was suggested to further improve the properties of the Ti-6Al-4V specimen.

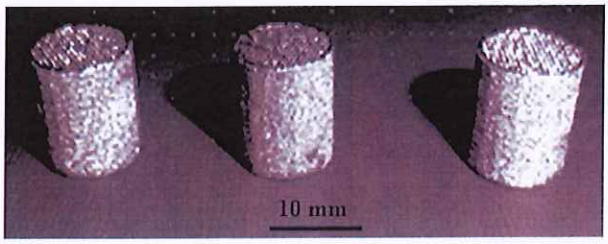

Fig. 14. Fabricated Ti-6Al-4V specimens with porous structure via SLM [100].

The post-annealed microstructures of Ti-6Al-4V specimen at 700, 750 and 799 °C temperature are shown in Fig. 8(a), (b), and (c), respectively. The images noticeably display the agglomerated, precipitated, and coarsened α lath. Meanwhile, Fig. 8(d) shows that the measured average thickness of α lath for as-printed parts is 0.327 ± 0.053 µm and increases to 0.647 ± 0.073 µm after annealing at 700 °C. The average α lath thickness further increases to 0.935 ± 0.104 µm at an annealing temperature of 799 °C. However, when compared with the post-annealed Ti-6Al-4V, the measured Vickers hardness value shows a slight difference. This is believed to be instigated by the change of the microstructure.

In terms of build direction, Radomila Konečná et al. [172] conducted a fatigue testing on DMLS printed Ti-6Al-4V alloy specimens oriented in three different directions. The investigation was conducted to understand the effect of the layered microstructure on the fatigue behaviour. The fabricated Ti-6Al-4V specimens underwent heat treated after printing to improve the static strength and reduce residual stresses through precipitation hardening. Their findings (Fig. 9) demonstrated a slight inclination in the shorter fatigue life for the Z-X specimen orientation. Fig. 10(a) shows the specific directional surface of DMLS printed Ti-6Al-4V specimen in 3D shape. The vertical arrow on the image shows that the build direction is in the Z-axis. From the figure, the two parallel surface planes on the cross sections of the layered structure are found to be in contrast with the structure on the top plane that is parallel to the plane of the laser beam movement. Moreover, the microstructural characterization also reveals a columnar elongated former β grains, formed parallel to the build direction. Thin needles of α stage in β lattice are also noticed inside these grains, as demonstrated in Fig. 10(b). The initial metastable α' martensitic is observed to be normal for "as organised" microstructure without heat treatment [173], but changes to a combination of $\alpha + \beta$ phases after the heat treatment. The α needles thickness was measured using the image analyser software and found to be around 0.5 µm. The thickness obtained was slightly higher as compared to the as-built specimen. Besides, an investigation by Baca et al. [174] on the material microstructure

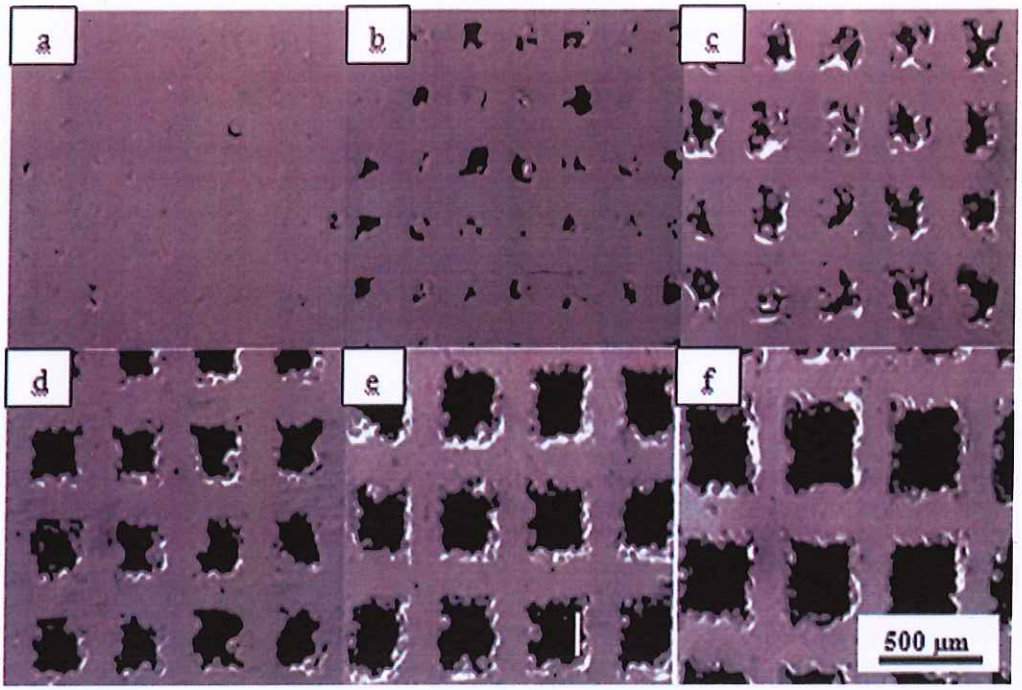

Fig. 15. SEM microstructures images at various scan lines distances: (a) 200, (b) 300, (c) 400, (d) 500, (e) 600 and (f) 700 µm of porous structured Ti-6Al-4V specimens fabricated via SLM [100].

produced through successive stress relief revealed lower laser power and temperature, which uncovered the existence of micro shrinkage.

However, the initiation of the fatigue crack was observed on the surface inverse to the notch. The single crack initiation for the specimen with X-Y and Y-Z build orientations is shown in Fig. 11(a) and (b), respectively. Meanwhile, Fig. 11(c) displays numerous crack initiations on the Z-X oriented specimen (arrow in the picture refers to the crack initiation). The initiation of the crack was reported to be dependent on the surface quality of the specimen. Fig. 11(d–f) reveal in detail the location of the crack initiation for three different oriented specimens. Thus, from the study conducted by other researchers [172], the suitable processing parameters to deliver an isotropic fatigue life material were identified to be 50 µm for layer thickness, 400 W for laser power, and 720 °C for heat treatment.

Todd M. Mower and Michael J. Long [175], in counterpart, studied the microstructure of DMLS Ti-6Al-4V in the section transverse to the long axis of unstrained tensile specimens and the section from the horizontal orientation that was perpendicular to the build plane. The horizontally-grown surfaces of the DMLS Ti-6Al-4V specimens are shown in Fig. 12. They witnessed a few pores that appeared in the modular asperities with a granular texture and solidified bead of melted powder in the "as-fabricated" specimen (Fig. 12(a)). However, the electropolished surfaces of DMLS Ti-6Al-4 V showed a brighter with smoother high points, while the low areas displayed a depression with no visible pits (Fig. 12 (b)). Nevertheless, the specimens developed in both (longitudinal and vertical) oriented axis showed a comparable structure.

Additionally, the microstructure of the investigated DMLS Ti-6Al-4V, as shown in Fig. 8(a), revealed the conventional Ti-6Al-4V dual-phase material with isolated lamellar $\alpha + \beta$ colonies interspersed among the nearly equiaxed and connected α grains with sizes that varied from about 15 µm to 30 µm. Whereas, Fig. 13(b) and (c) display the sections of the DMLS Ti-6Al-4V that exposed the long, slender needle-like (acicular) grains. A similar Ti-6Al-4V structure created by DMLS was identified earlier as a fully martensitic α' phase [176]. Whereas, Fig. 13 (d) shows the microstructure of the Ti-6Al-4V treated with the HIP. The outcome demonstrated the formation of elongated grains with greater alpha lath thickness after the HIP treatment.

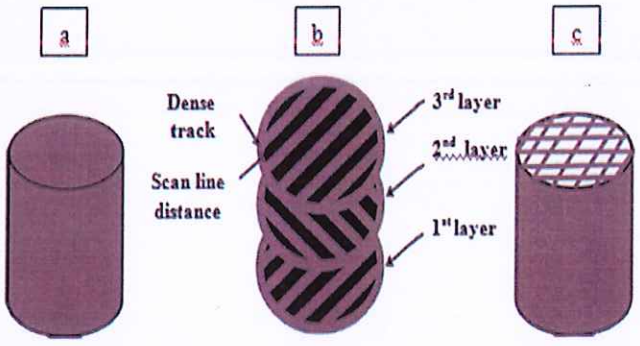

Fig. 16. Graphical illustration of adjusting scan line distance of Ti-6Al-4V specimens with porous structure: (a) 3D model, (b) strategies of scanning, and (c) layer loading to obtain the end dimensions [100].

4. Ti-6Al-4V by using Selective Laser Melting (SLM)

The porous Ti-6Al-4V implants fabricated by using SLM were substantiated to be suitable for in-vitro cell applications [177,178]. Currently, several practices are presented and adapted to produce excellent repetition and porous implants control via SLM. The 3D model design of the porous structure is usually developed by using CAD software. Structures like mesh scaffolds, analogue porous bone models, and other porous bones were investigated in many studies [46,47,179–181]. Several other researchers have also attempted to attach carrying agents on the metallic powders to produce honeycomb-like pores with specific pore sequences [182]. Principally, fabricating metallic implants is not an easy task, as developing complex porous metal structures poses another level of difficulty [183]. However, by controlling precisely the process parameters, porous metal structures

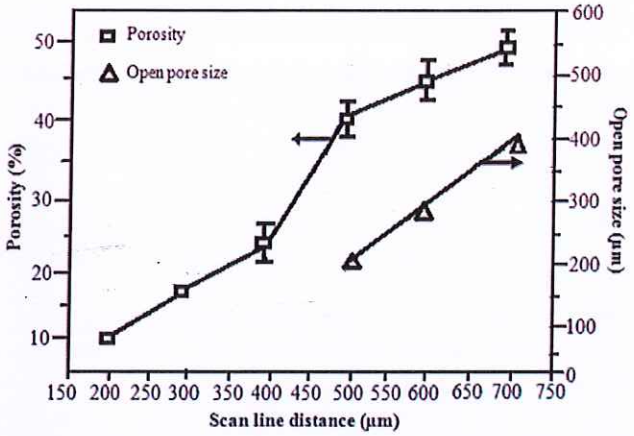

Fig. 17. Pore size and porosity of the porous Ti-6Al-4V specimens at different scan line distances [100].

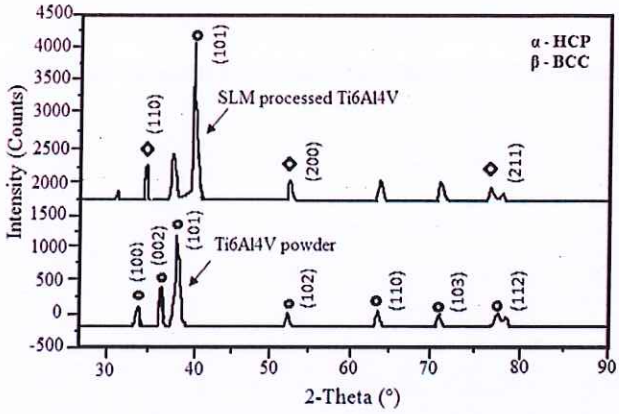

Fig. 19. XRD spectrum of SLM-processed and as-received Ti-6Al-4V [100].

can be easily attained using the SLM technique [184,185]. Other than being cost-efficient, this approach also saves a significant amount of manufacturing time and offers the feasibility of customising a variety of challenging configurations [176,186,187].

4.1. Microstructure of Ti-6Al-4V by SLM

Sheng Zhang et al. [100] investigated the effect of scan line spacing on the produced Ti-6Al-4V specimens. The Ti-6Al-4V specimens image fabricated by SLM is depicted in Fig. 14. The entire cross-section profile of the specimen can be seen from the side, while the pores are at the top surface of the figure, respectively. Fig. 15 shows the normal and rectangular-shaped pore distributions with thin wall struts of approximately 200, 300, 400, 500, 600, 700 μm in size for each specimen.

The diagram in Fig. 16 shows the analysis and scanning strategies used to obtain the end dimension of Ti-6Al-4V specimens. It was clearly observed that the single laser scan line of approximately 200 μm spot size caused the thin wall struts. Also, through scan line distance modification, the length of exceeding 200 μm as required by the pores was attained. Fig. 15(a) shows the resulted closed pores with irregular shapes of about 200 μm of scanned line distance. However, when the pore diameter is smaller than the largest powder size, it becomes an open pore. Fig. 15(b) shows the pores that fail to open after the laser scan line distance is increased to 300 μm. Meanwhile, the image in Fig. 15(c shows some of the pores were still connected. However, as the pore size increases with scan line distance approaches 400 μm, nearly all pores became closed. The unsatisfactory pore sizes, i.e. not sufficiently large, will not be occupied by powder particles and the render is disconnected. The image in Fig. 15(d) shows the developed pores as the scan line distance is increased to 500 μm. Whereas, Fig. 15(e) and (f) show the formed interconnecting pores with sufficient space for powder passing at 600 and 700 μm, respectively. The outcome of this investigation proved that an implant requires a scan line distance of larger than 500 μm to form interconnected pores for practical applications, whereas the lower spot size can be used to control the thin wall width for the implants. The relation between the diameter of the open pore size and porosity by using line scanning distance is illustrated in Fig. 17. It is observed that the porosity increased linearly as the scan line distance is increased. A commonly accepted understanding is that the implants require highly porous yet organised structures [86].

It was proven that the porous structure of the implants can be improved by manipulating the scan line distances and the porosity can be designed to suit the patient's requirement. Also, these implants are shown to improve the biological fixation to reach durability and stability in vivo. However, the potential harmful ramifications of scan line spacing are the pore allocation that would be strongly dependent on directional solidification and formation of rough surface pores. The typical microstructure of Ti-6Al-4V fabricated by SLM and the as-received Ti-6Al-4V powder are shown in Fig. 18. The Ti-6Al-4V specimens made through the SLM technique and the as-received alloy powder contain a mixture of α and β phases in their microstructure. Additionally, the Ti-6Al-4V specimen fabricated by using SLM incorporates an enhanced needle-shaped β phase. These were verified by the X-ray diffraction (XRD) analysis (Fig. 19) conducted on both SLM and as-received Ti-6Al-4V alloy powder.

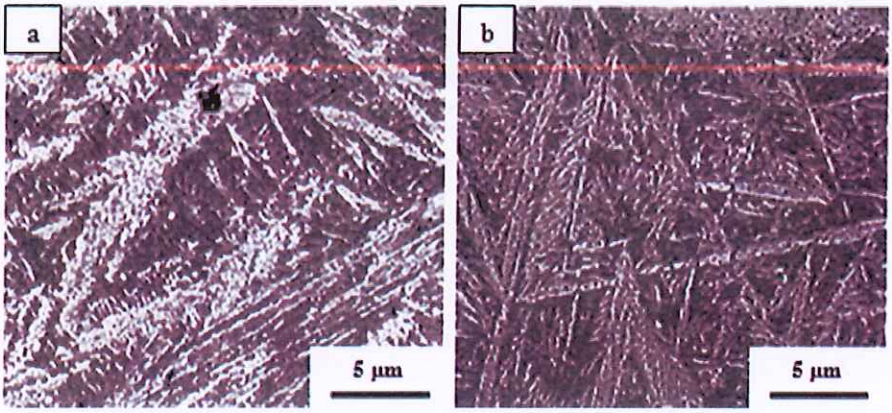

Fig. 18. Microstructure characteristic of (a) laser procedure specimen and (b) as-received alloy powder [100].

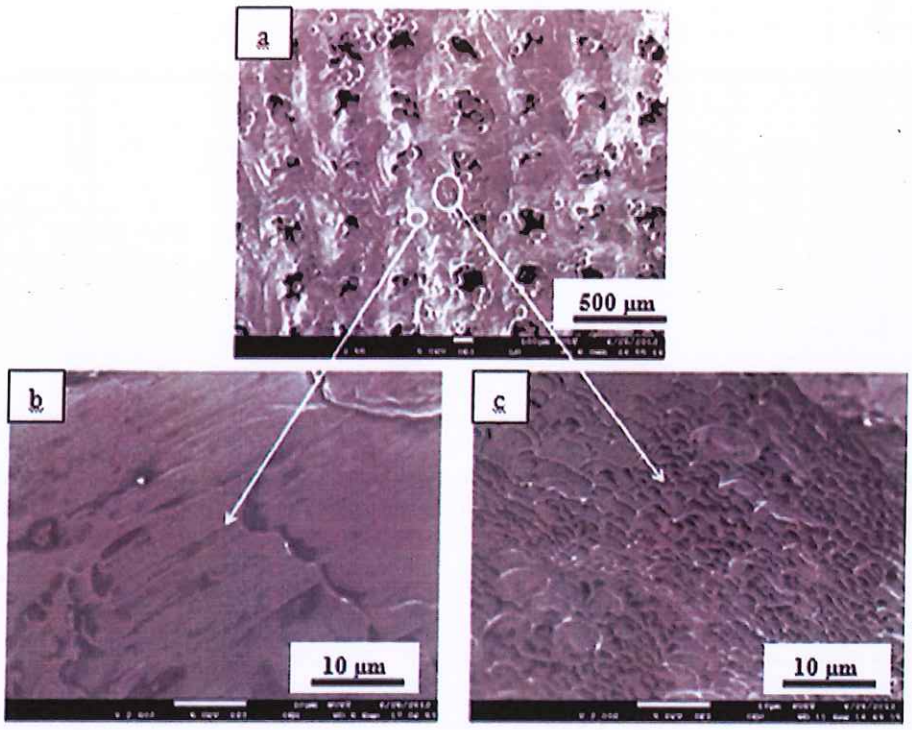

Fig. 20. Microstructure of porous Ti-6Al-4V specimen with typical rupture exterior [100].

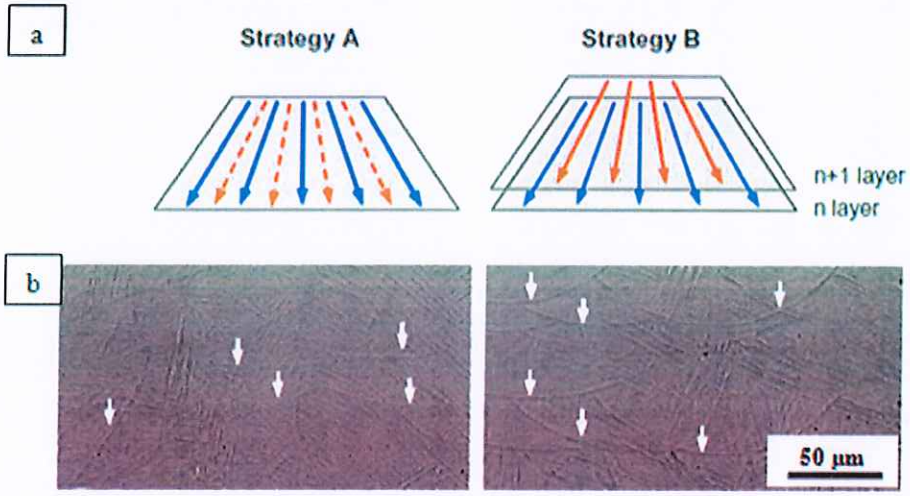

Fig. 21. (a) SLM scanning strategies on Ti-6Al-4V specimen and (b) SEM microstructures of scanned specimens (the white arrows show melt pool boundaries) [198].

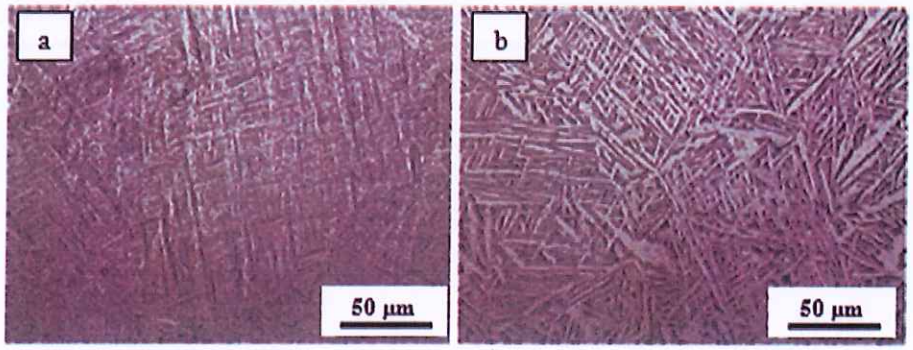

Fig. 22. Microstructure of SLM Ti-6Al-4V specimens in the (a) as-built condition, and (b) after the HIP treatment [200].

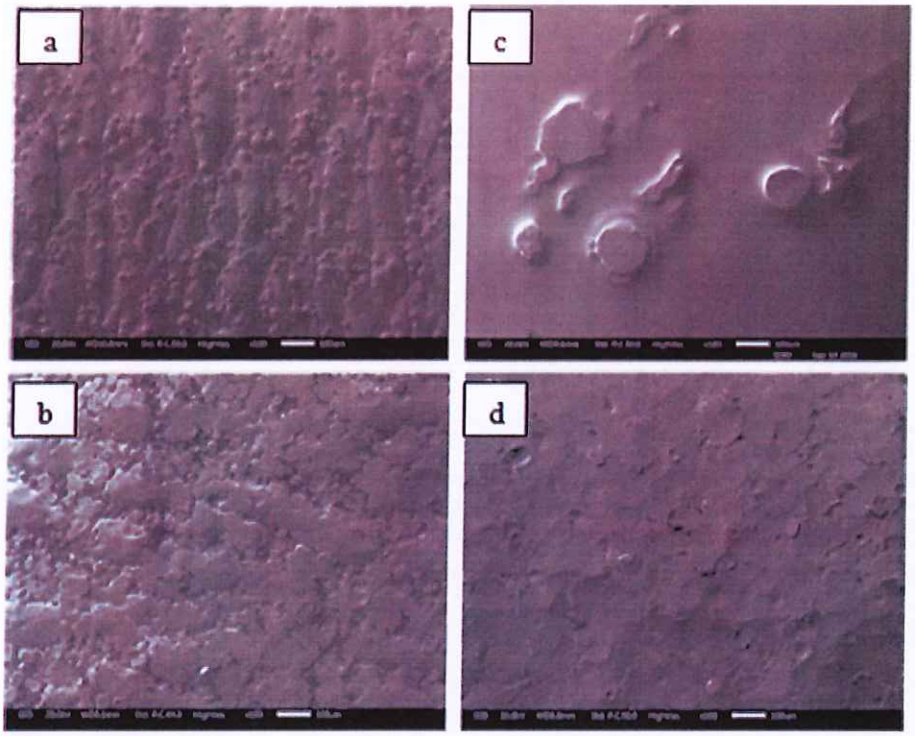

Fig. 23. SEM micrographs illustrating the surface morphology of the specimens. (a) as-built, (b) tribofinished, (c) electropolished, and (d) shot peened [200].

Poondla et al. [188] and Sun et al. [189] had further analysed the SLM-produced specimens by heating them at conversion temperature. Subsequently, the specimens were cooled at different cooling rates and followed by the particle morphology analysis. From their studies the particle morphology was found to have similar microstructure. The initial microstructure of the SLM-fabricated Ti-6Al-4V specimens

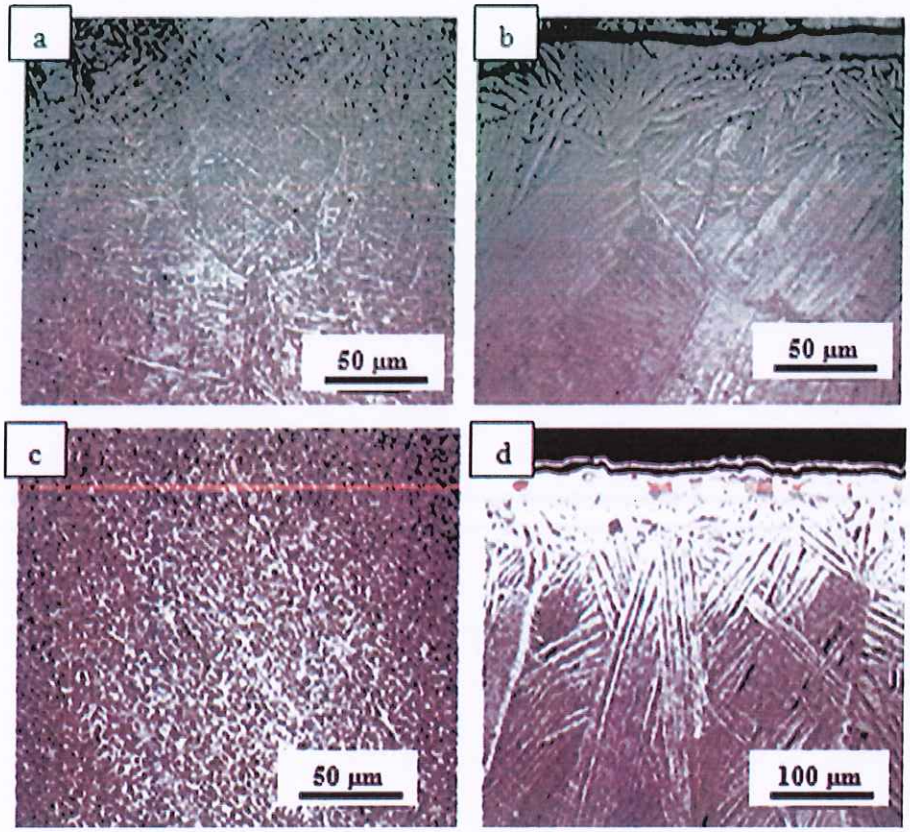

Fig. 24. Optical microstructure image for: (a) EBM Ti-6Al-4V, (b) cast Ti-6Al-4V, (c) wrought Ti-6Al-4V, (d) cast cp-Ti [113].

was exposed to be in martensitic phase. Vrancken et al. also obtained similar results in their research [176]. During rapid cooling, for example, at the rate of exceeding 103 K/s, the *V* atoms of the solid Ti-6Al-4V phase β do not have sufficient time to diffuse from the unit cells hence it is transformed to phase α. Therefore, the phase β raised by SLM fabrication process through the conversion of martensite is a diffusionless transformation [190]. There is no stable bonding or accidental breach of the atom through the boundary. Hence, the martensitic phase is believed to conquest the atomic order, chemical composition, and the crystal defects of the parent specimen.

The microstructure of a porous Ti-6Al-4V specimen with a typical exterior rupture (200 μm scanned line distance) is shown in Fig. 20, while the microstructure analysis of the Ti-6Al-4V specimens are shown in Fig. 20(b) and (c). From the micrograph a dimple-structured characteristic of the specimens can be observed. Normally, the SLM-produced Ti-6Al-4V is ductile. However, it is still possible to experience brittle failure due to the deformation of concentrated local stress and temperature increase that resulted from the different cooling shear bands. It was also expected that adiabatic shear band (ASB) formation is possible especially on titanium metal alloys [191]. Previous studies have proved that failure is indeed possible as a consequence from additional thermal softening which promotes the ASB development [192]. Besides, the pores also could potentially act as an initiation location for the ASB development.

Mullen et al. [193,194] had successfully manufactured porous titanium alloy specimen in their studies by using SLM technique and investigated the geometric effect of the unit cell on the produced specimen mechanical properties. They demonstrated that porous material with arbitrary porosity and good compressive strength can be achieved using the SLM process. Furthermore, Stamp et al. [195], Douglas T. et al. [196], and Warnke et al. [197] were all in agreement with Mullen et al. in manufacturing porous titanium alloy via SLM technology for biomedical applications. I. Yadroitsev et al. [198] alternatively introduced two different scanning strategies to fabricate Ti-6Al-4V via SLM as illustrated in Fig. 16. The "two-zone technique" (strategy A) [199] determines the highest density specimens, whereas, the second approach (strategy B) reduces the effect of the Heat-Affected Zone (HAZ) and re-melting number of the final microstructure. Fig. 21(a) shows the smooth microstructure morphology of the as-made SLM specimens categorised as a α' martensitic [149], while Fig. 21(b) shows the observable melt pool boundaries of the tracks resulted from the different mechanical properties of the materials. The heating and cooling processes above the β-transit temperature ($T_{\alpha\text{-}\beta} = 1000 \pm 20$ °C) guide the re-nucleation of the complete phases since the cooling rate is dependent on the alteration of β-phase.

M. Benedetti et al. studied the effect of post-sintering treatments on the fatigue and biological behaviour of Ti-6Al-4V specimens made by using SLM technique [200]. Fig. 22 reveals the microstructure of the different experimental conditions studied. Fig. 22(a) shows the microstructure of "as-built" condition specimens after the stress relief. Usually, after the fabrication process, heat treatment is performed to modify the microstructure or reduce the residual stresses. Fig. 22(b) shows the microstructure after the HIP treatment. From the investigation, it can be observed that the α' phase changed into $\alpha + \beta$ phase without any grain growth after the heat treatment. The development of final lamellar microstructure was reported due to the diffusional $\beta \rightarrow \alpha$ conversion with lamellas of α phase in a β phase.

The micrographs in Fig. 23 show the fabricated specimen's external surface morphology obtained from SEM imaging. Fig. 23(a) shows the unfused particles observed along the specimen's built direction. Whereas, the image in Fig. 23(b) shows the smooth surface of the specimen with an intense plastic deformation and abrasion of the unfused powder after the tribofinishing process. Fig. 23(c) shows the electropolished surface that is smoother with small remnants of unfused particles. Meanwhile, the image after shot peening, as presented in Fig. 23(d), shows the formation of more uniform surfaces with impact dimples. Finally, the HIP treatment (not shown for the sake of brevity) generated a smoother surface as compared to the shot peened and without the presence of surface dimples.

5. Ti-6Al-4V by using Electron Beam Melting (EBM)

To date, numerous investigations have been performed to study the performance of the Ti-6Al-4V parts produced by EBM technique [201–207], such as the development of femur-hip implants [208], titanium root structure implants [209], invention and strength classification of porous Ti-6Al-4V formations [207,210], premature bone reactions in rabbits [211], "in-vivo" performance of the porous Ti-6Al-4V structure [212], evaluation of the titanium implants for "in-vivo" applications [213], titanium implants for "in-vivo" in contrast to conventional cast implants [214], and "in-vitro" biocompatibility of Ti-6Al-4V implants [215,216]. In the earlier studies, Harrysson et al. used direct metal manufacturing to produce titanium implants and later tailored them by employing EBM for customised mechanical properties [208]. Meanwhile, Christensen et al. [217] successfully prepared the Ti-6Al-4V ELI specimens using EBM with a few modifications in the fabrication process. Whereas, Murr et al. [218,219] conducted a complete investigation on the mechanical properties and the resulted Ti-6Al-4V microstructures fabricated using EBM. The tensile properties of the Ti-6Al-4V ELI manufactured by the EBM technique was found to be superior as compared to the conventionally built specimens [209].

5.1. Microstructure of Ti-6Al-4V by EBM

The microstructures of the fabricated Ti-6Al-4V specimen using EBM process are shown in Fig. 24(a) and (d). The microstructure was analysed from the specimen's surface perpendicular to the assembly path of EBM. The micrographs of Ti-6Al-4V ELI and cp-Ti showed that the microstructures were similar with the surfaces of the casts (Fig. 24(b) and (d)). A small degree of dissimilarity can be observed on structural fineness. The basket weave and widmanstätten microstructures were observed in α titanium platelets which were absent in the wrought specimens, whereas, from the cp-Ti micrograph in

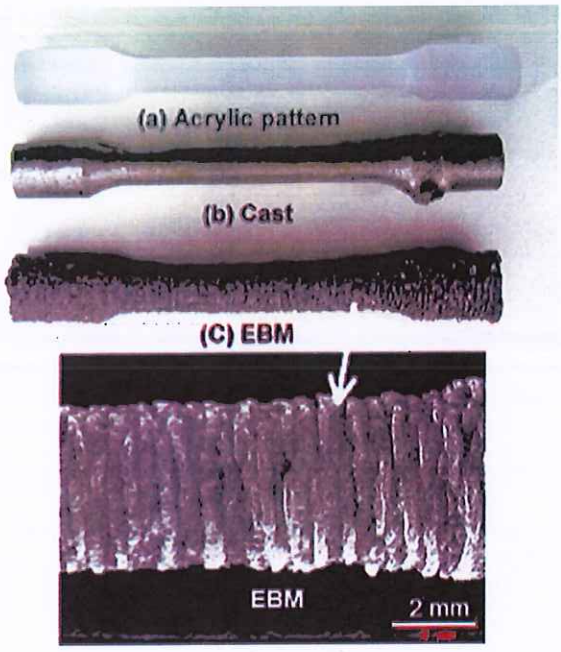

Fig. 25. Exterior surface of (a) dumbbell specimen made of plastic, (b) cast Ti-6Al-4V specimen, and (c) EBM Ti-6Al-4V processed specimen [113].

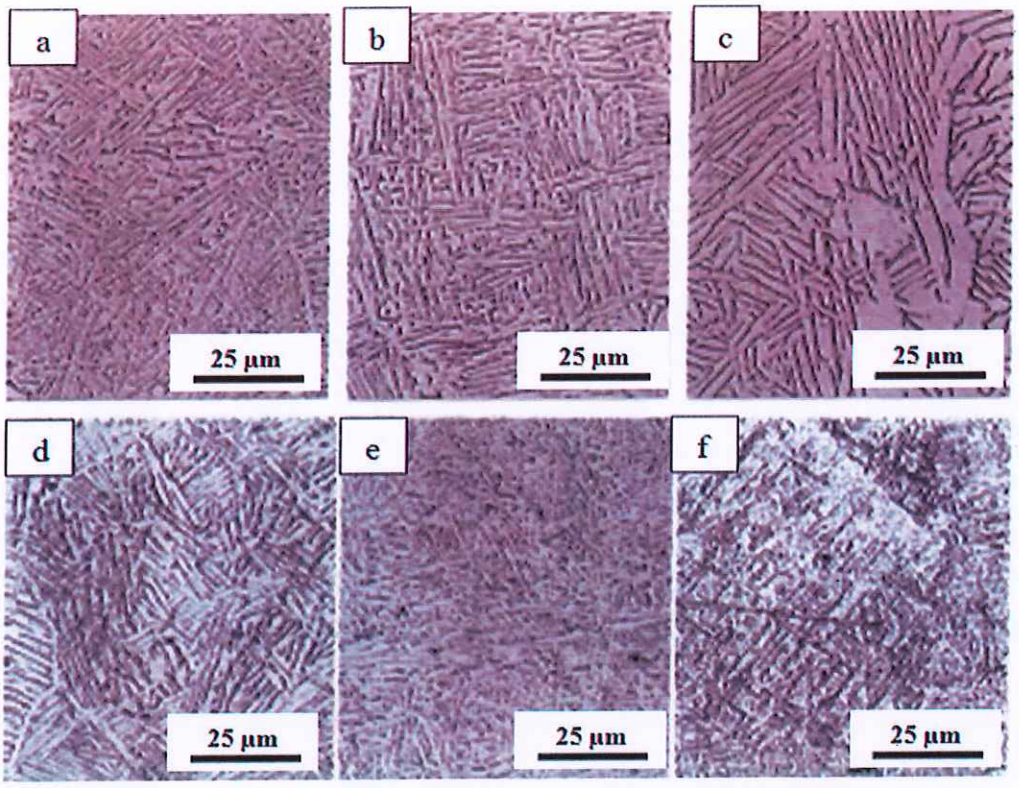

Fig. 26. Microstructure images (a–c) for different thermal processing conditions for EBM Ti-6Al-4V: α-phase acicular grains increasing in thickness from 3, 4. 5, and 6 μm melt passes for cm thick specimens, the decreasing of α-phase thickness (d) for mm thick specimens for top and (e) bottom, and (f) 1 pass in creating ~2 μm spaced α-phase platelets from rapid cooling effect [221].

Fig. 24(d), a typical microstructure of α-case comprising columnar α crystals was seen in the cast specimens. However, no α-case was discovered near the surface of EBM-manufactured specimens. Meanwhile, the wrought Ti-6Al-4 V ELI microstructure (Fig. 24(c)) shows the existence of intergranular α grains and moderately elongated α grains after heat treatment [220].

The ability to produce an excellent surface structure for biomedical application as compared to the traditional method is one of the EBM's unique characteristics. A comparison between the external surfaces of a Ti-6Al-4V ELI specimen built using EBM technique and casting is shown in Fig. 20. From the figure, the waved-layers with several unutilised alloy particles attached to the surface observed in EBM specimen were the results of repetitive melting and sintering of the alloy powders. These waved surfaces of the EBM-fabricated alloy are preferred in various applications such as dentistry (Fig. 25).

Lawrence E. Murr and Wayne L. Johnson [221] investigated the microstructure of Ti-6Al-4V specimens fabricated via EBM technique at different thermal processing conditions. The microstructure images obtained from the study are shown in Fig. 26. The finding specified that each melt pass increased the average thickness (width) of alpha-phase lenticular grains from 3 μm (Fig. 26(a)) to 4.5 μm (Fig. 26(b)), and 6 μm (Fig. 26(c)). The increase in average thickness was believed to be caused by an equivalent decrease in the hardness as shown in Fig. 26(a)–(c). Besides that, it was also noticed that as the cooling rate of specimens increased (Fig. 26(d)–(f)), the lenticular alpha grain width decreased as well (Fig. 26(d)–(e)). These were believed to be due to the heating and annealing steps during specimen manufacturing. Moreover, the conversion from alpha (Fig. 26(a)) to alpha-prime phase (Fig. 26(f)) resulted in about 40% of hardness increase owing to the rapid cooling in the foam ligament.

Greitemeier, D. et al. attempted to improve the fatigue performance of DMLS Ti-6Al-4V [160]. They evaluated the microstructure at two different post-treatments. The image in Fig. 22 shows the obtained microstructures at two different post-treatments of Ti-6Al-4V specimens. It

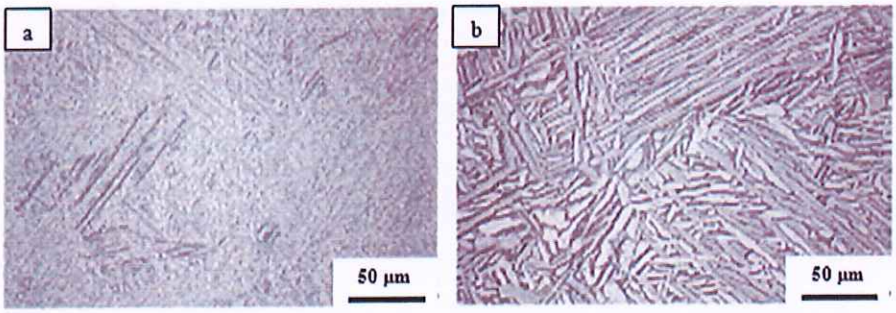

Fig. 27. Microstructure images of DMLS Ti-6Al-4V: (a) annealed and (b) HIP [160].

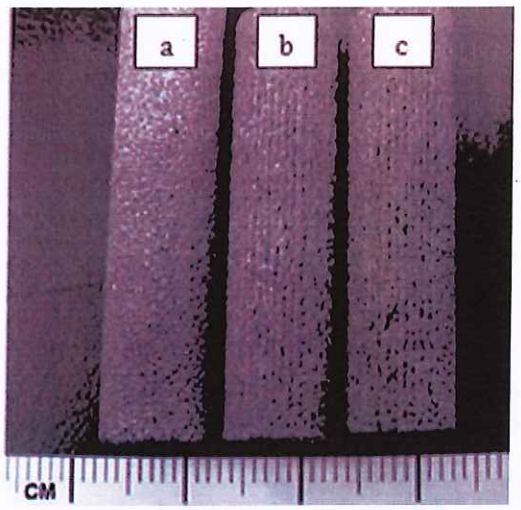

Fig. 28. The characteristics of porous Ti-6Al-4V specimens manufactured using LENS. Total porosity (a) 17, (b) 23 and (c) 30% [122].

was not specified whether the fine acicular microstructure observed for an annealed specimen (Fig. 27(a)) contained α' (martensitic) or α. However, the formed acicular could happen due to the quick solidification and lower heat input during the build-up and heat treatment. Fig. 27(b) shows a considerable coarsening of the lamellar microstructure for the HIP DMLS Ti-6Al-4V specimens. However, it has to be clear that a definite difference could not be observed between both phases due to the comparable crystalline structure. The size, amount, and shape of the pores for both samples were investigated by using computer tomography. The measured pore sizes of the annealed specimen were <240 μm. However, after HIP treatment, the pores were unnoticeable for the DMLS Ti-6Al-4V specimens. Meanwhile, Guo, M. et al. developed a novel composite scaffold consisting of porous Ti-6Al-4V specimen filled with chitosan sponge using a combination of EBM and freeze-drying techniques. The outcomes from the investigation concluded that the low stiffness and good mechanical strength for porous Ti-6Al-4V specimens fabricated by EBM method was extremely suitable for biomedical implants [222].

6. Ti-6Al-4V by using Laser Engineered Net Shaping (LENS)

The Ti-6Al-4V specimens fabricated by LENS technique are shown to have greater critical tensile strength, elongation, and yield strength as compared to annealed or specimens fabricated by other traditional methods [223]. Amit Bandyopadhyay et al. used the Ti-6Al-4V alloy produced via LENS to investigate the compression and microstructural properties [122]. Two different levels of laser power were used to partially melt the metallic powder through a deposition process for producing specimens with a porous structure. They also used different processing parameters, such as scan speeds and powder feed rates, to examine the influence of parameters on material porosity [122]. There were also other researchers that studied about Ti-6Al-4V by using LENS [39,224–228].

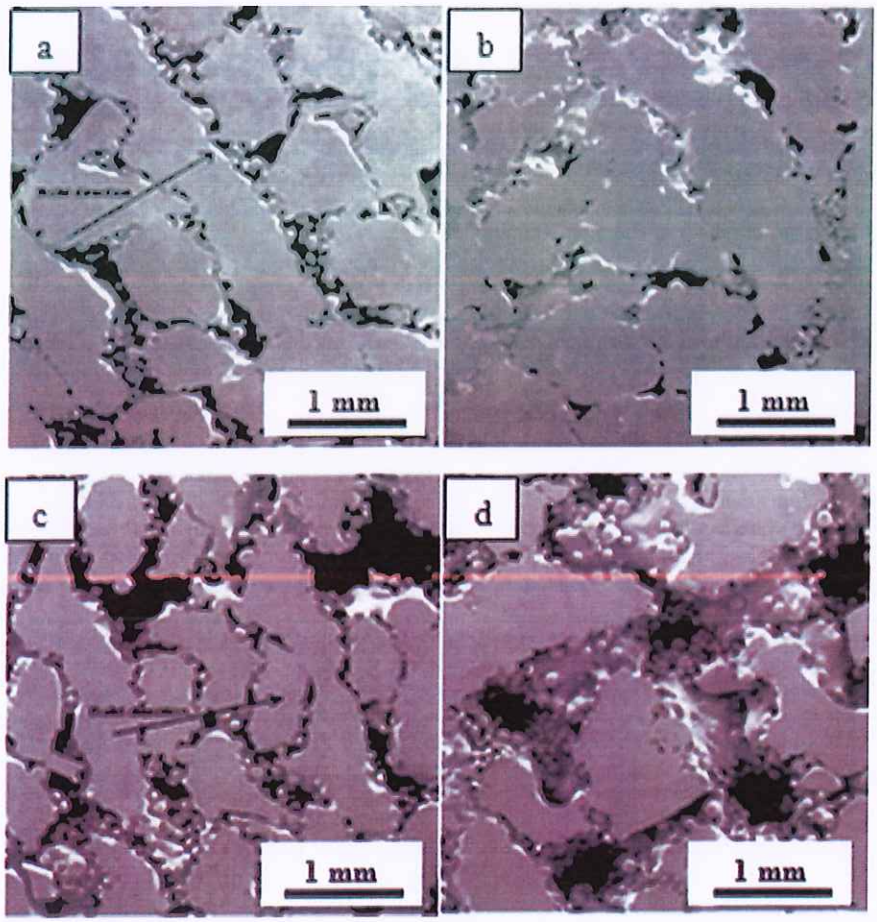

Fig. 29. The micrograph for pore connectivity (the arrows show building direction) [122].

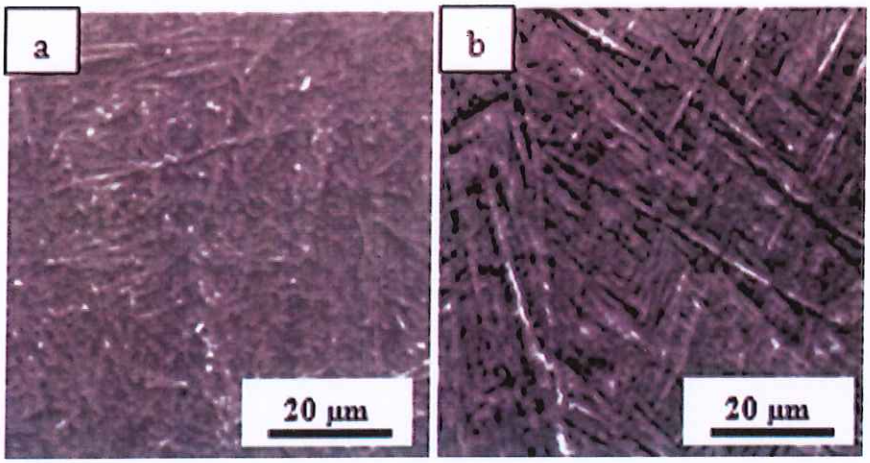

Fig. 30. The microstructure characteristics of: (a) as-received powder, (b) laser-processed specimen [122].

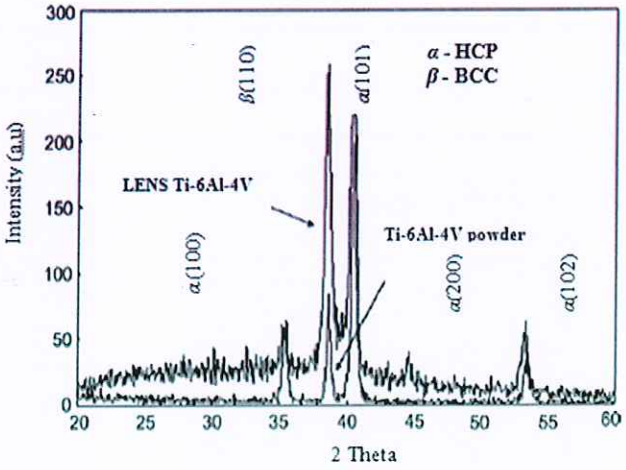

Fig. 31. XRD spectrum of as-received Ti-6Al-4V alloy powder and laser-processed Ti-6Al-4V alloy specimen [122].

6.1. Microstructure of Ti-6Al-4V by LENS

Fig. 28 displays different porosity characteristics of Ti-6Al-4V specimens manufactured by LENS. The analysis displayed an open porosity surface with bulk density that varied from 67% to 85%. The bulk density of the specimens produced by LENS often relies on manufacturing parameters. However, the interconnectivity of the pores were observed to be diversed in different directions as shown in Fig. 29. The pores in the build direction (shown by the black arrows) were seen to have more connectivity as compared to the pores acquired perpendicular to the build direction, as shown in Fig. 29(a) and (b). Regardless of the pores connectivity, the surface of the samples were found to be comparatively homogeneous on both tracks with the density reduced by approximately 75%, as illustrated in Fig. 29(c) and (d).

Fig. 30 shows the matrix microstructures of the porous specimen fabricated via LENS and as-received Ti-6Al-4V metal powder. Both LENS Ti-6Al-4V and as-received Ti-6Al-4V metal powder exhibits a combination of microstructures which consisted of α and β specimens.

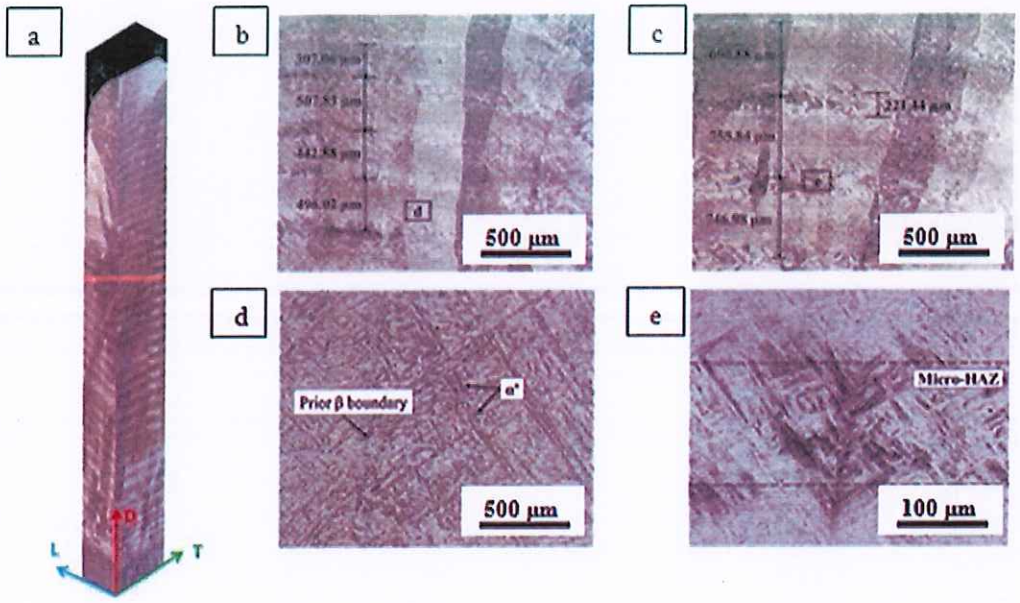

Fig. 32. Microstructure of LENS Ti-6Al-4V: (a) panoramic view of the build-up from cross sections of a 40 mm tall deposition, (b) different layer thicknesses (thinner at the bottom), (c) different layer thicknesses (thicker at the top of the build), (d) fine martensitic microstructure, and (e) coarser microstructure within micro-HAZ [229].

Fig. 33. Panoramic vision of: (a) fatigue fracture surface and (b) side profile of the crack path [229].

However, the LENS Ti-6Al-4V was observed to have the needle-formed β phase. Fig. 31 demonstrates the XRD analysis conducted on LENS Ti-6Al-4V and as-received Ti-6Al-4V metal powderfor specimens. The finding revealed the existence of a significant amount of β phase at high-temperature.

However Hayley R. Sandgren et al. reported a different mechanism for confining the development of small fatigue cracks in LENS Ti-6Al-4V [229]. The resultant microstructure was observed to contain large columnar β grains (about 1–20 mm long and 0.2–4.0 mm wide) perpendicular to the substrate, as shown in Fig. 32(a). Figs. 32(b) and (c) respectively display the layer bands with layer thickness of 300 μm and 800 μm (calculated using the image analysis software). Whereas, Fig. 32(d) shows the fine α' phase (5–20 μm long and ~0.7 μm thick) observed inside the columnar grains caused by fast cooling, and Fig. 32(e) displays a coarser microstructure among the layers which resulted from the re-heating or re-melting of the previous layers.

The reported fatigue crack growth (FCG) data were obtained from 2D and 3D tomography renovations, while the fracture length measurements were obtained from SEM. The panoramic vision of the fatigue fracture surface observed using SEM is illustrated in Fig. 33. The white mark in the image shows the end of fatigue failure. By separating the fatigue fracture surface (region connecting the first notch and the white line), the tensile load fracture surface can be observed (the region outside the white line). The findings also indicated that the crack propagation occurred inside one of the columnar β grains.

The microstructure analysis of the fatigue fracture surface was performed by using SEM at different ΔK values, which can be observed in Fig. 34. Fig. 34(a) shows the cleavage steps or planes specifying the occurrence of brittle failure near the notch, which is related to the long FCG threshold. Fig. 34(b) shows the ductile fracture at higher ΔK and Fig. 34(c) demonstrates the branching of the crack. In conclusion, the fractographic analysis and X-ray microtomography can be effectively united to understand the propagation of fatigue cracks in the LENS Ti-6Al-4V specimens.

Zhai et al. studied the behaviour of long and small fatigue cracks propagation on Ti-6Al-4V fabricated using LENS [230]. The long fatigue crack growth (FCG) in the tensioned specimens were assessed using conformity method to observe the crack propagation. The surface flaw tension experiment was developed for small FCG, and the crack growth was captured using direct current potential drop (DCPD) technique. Fig. 35(a) demonstrates both small and long FCG data obtained and collectively plotted with the data from conventional mill-annealed Ti-6Al-4V. Fig. 35(b)–(d) show the lower and higher fracture toughness values of the LENS-fabricated specimens. The small FCG data obtained indicated the acceleration and retardation of crack growth rates due to the microstructural features. Fig. 35(e)–(f) show that the LENS Ti-6Al-4V specimens contained β columnar grain boundaries.

7. Current trends of metal-AM

Additive manufacturing (AM) technique supports in optimising invention evolution time and fundamental aspect of the specimen design [231–234]. Although the AM offers numerous benefits than conventional manufacturing technologies, several limitations still exist, which include for instance, dimensional accuracy, staircase effect, and surface quality of the produced specimens. To date, many studies have been conducted to overcome these shortcomings [87,235–237]. There are a variety of post-processing techniques (conventional and non-conventional approaches) to minimise the limitations of the metal-AM processes [238,239].

The metal-AM technique has steered the development of new, modern, and superior technologies and procedures [230,240–243] and it is adopted in broad applications including the biomedical applications, i.e., for knee and hip implant fabrications [244,245]. Fig. 36 exemplifies the various types of fabrication methodologies for the production of metal alloys parts for biomedical applications. From these studies, there were about 57% of industries which employed metal-AM technique to produce biomedical metal specimens in the year 2000 to 2017. Whereas, the conventional methods, such as machining and casting recorded about 2 and 7.5%, respectively and meanwhile MIM ranked second with 33.5%. The findings indicated metal-AM as the frequently opted technique to fabricate metal alloys for biomedical applications, even for conventional applications. This is due to the capability of the metal-AM technique in producing superior properties and porous specimen that are crucial for biomedical implant development. The trend of metal fabrication using additive manufacturing is illustrated in Fig. 37 which clearly indicates the growing trend of metal-AM processes in the manufacturing of biomedical devices from 2000 to 2017. In the early 2000s, metal-AM was reported as a non-preferred method, however, it gained popularity with the rise of the biomedical industry. This

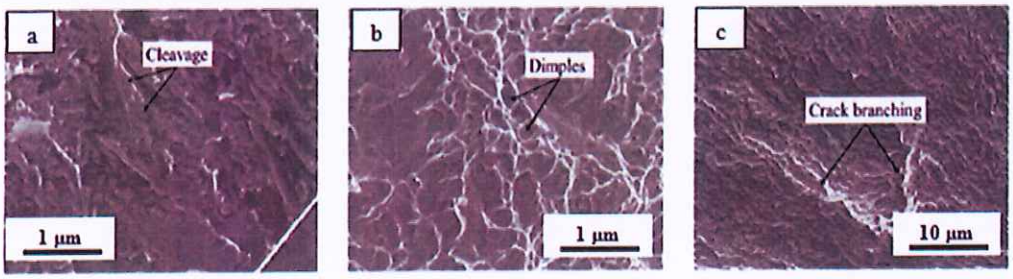

Fig. 34. SEM microstructure image of: (a) elements of cleavage steps or planes representing brittle behaviour through crack propagation, (b) end of an experiment demonstrating the ductile fracture, and (c) crack branching [229].

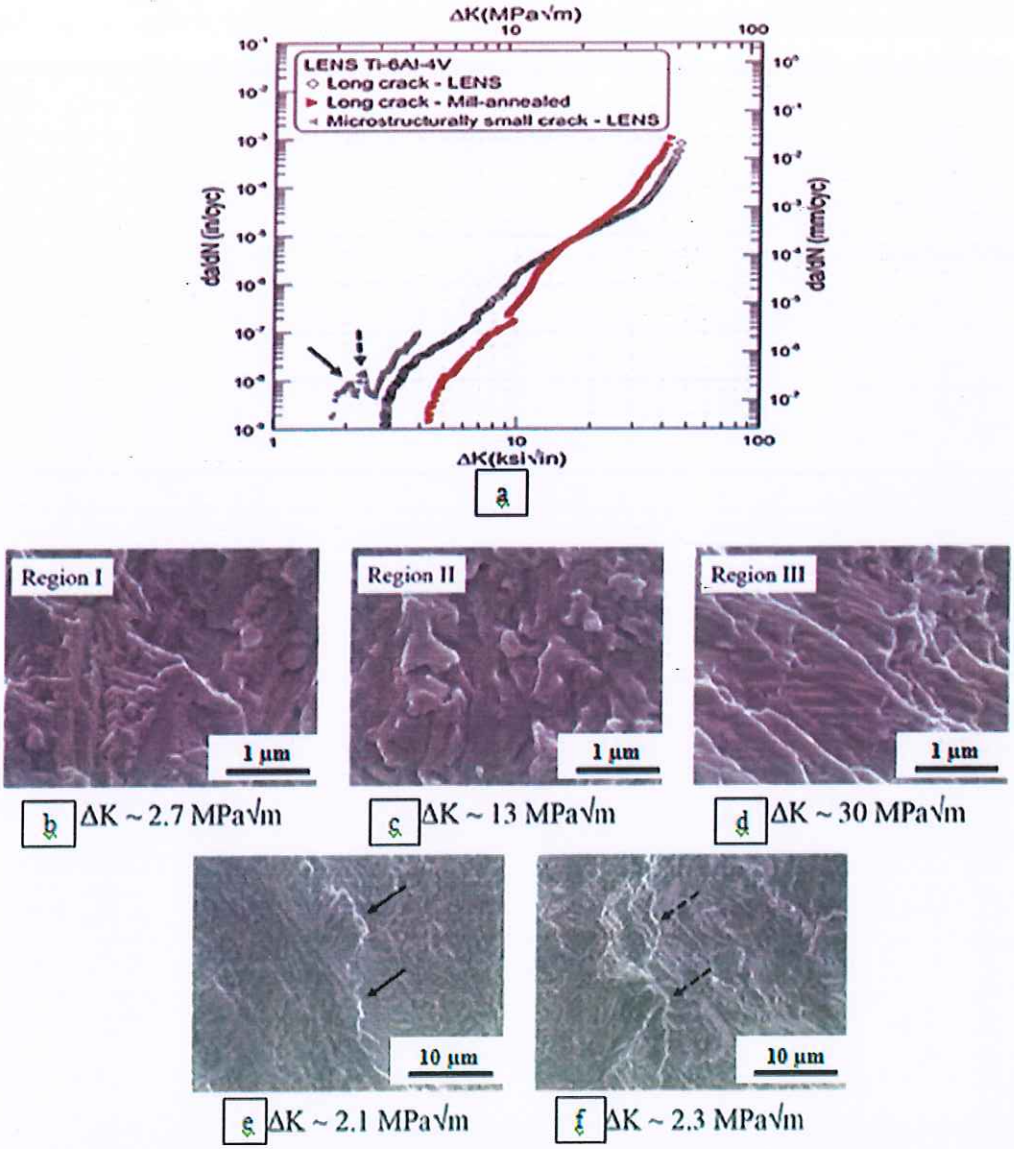

Fig. 35. (a) Long and small FCG data of Ti-6Al-4V LENS examined at $R = 0.1$, compared to mill-Ti-6Al-4V, (b) fractography of long FCG threshold, (c) Region II, (d) Region III, and (e)–(f) fractography on confirmation of small cracks related to β grain boundaries at the development and retardation points (pointed by the arrows) [230]

can be noticed from the trend starting in the year 2000 until 2006, where the percentage of metal-AM process utilisation increased from none to 3.6% and proliferated from the year 2006 to 2008 with increment from 3.6 to 7.1%. The use of metal-AM in biomedical application increased to 23.7% in the year 2014. The significant growth of metal-AM can be observed in 2014 and onwards, where the graph demonstrates the highest percentage of utilisation related to metal-AM

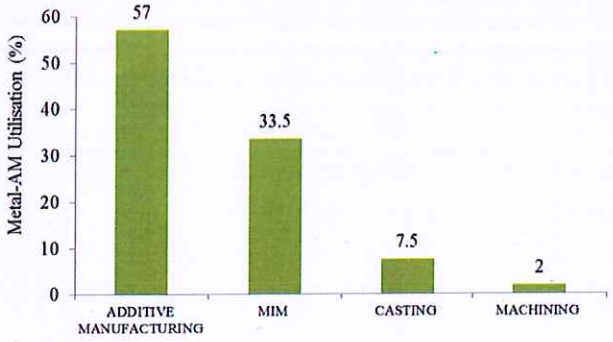

Fig. 36. Metal alloys fabrication by various techniques for the years between 2000 and 2017.

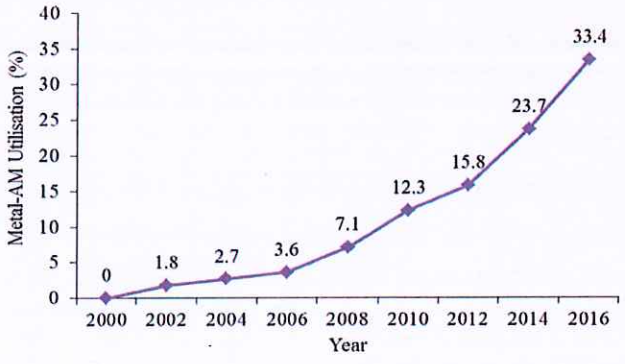

Fig. 37. Trend in utilisation of metal-AM for biomedical applications for the years between 2000 and 2017.

processes. Furthermore, the metal-AM technology gained interest not only in the perspective of academic purposes but also in industrial applications. The trend was in fact supported by several other findings by various researchers [246–248].

Besides that, another new approach is starting to gain popularity which is insitu manufacturing [249–255]. This technique is identified as the future of metal-AM technique for biomedical applications [250,256]. This method is categorised as a novel approach as the implants, or living organs are printed alongside (concurrently) in the body during the actual surgery is being performed. Currently, the technique is being used to repair external organs such as replacing the human skin [257] of which a wound is filled with various fabricated cells. Cohen et al. managed to print alginate into severe osteochondral defects in a calf's femur model [256]. The in-situ production uses the metal-AM technique and targets to have a huge prospect for biomedical applications. However, this method is still in its infancy with considerable challenges to overcome. Another latest innovation in additive manufacturing technology is the Desktop Metal technology. Its latest production machine is being developed to work safely and rapidly to mass-produce metal components and does not necessitate any particular engineer to operate the equipment all the time. This technology is intended to work with a specialty furnace along with the MIM powders. By combining microwaves and conduction, the components are debound and sintered much more rapidly than in a conventional conduction furnace. Moreover, the ovens are cloud attached and rely on the software that modifies the sintering programme to the geometry of the component. This certifies a consistent shrinkage throughout the components. The Desktop Metal production unit works 100 times faster than the existing technology, manufacturing up to 8200 cm^3 of metal components per hour [258–261].

8. Conclusions

Metal additive manufacturing (metal-AM) techniques are considerd as the most promising methods to process Ti-6Al-4V alloy for biomedical applications. The techniques have also resolved several recurring issues in the manufacturing of porous and unitised components, for instance improving the interfacial connection of implants and host tissue, abating load-bearing problems, stress shielding, poor osseointegration, wear-induced bone loss, and enhancing in-vivo lifespan. The desired microstructure including the pore characteristics and porosities of a component can be precisely altered to suit numerous applications in the biomedical industry. Moreover, metal-AM techniques have also made possible the manufacture of various other metallic materials with excellent biocompatibility. The prime advantage of metal-AM technology is the ability to fabricate specialised Ti-6Al-4V alloy implants to meet individual patient requirements, and manufacture net-shaped metallic biomaterials.

Acknowledgements

Universiti Malaysia Pahang (www.ump.edu.my) fully supports the facilities and resources for this research. The authors would like to acknowledge their support for the Universiti Malaysia Pahang internal grants (RDU160337, GRS1503145, GRS1503121, RDU140354, RDU160354, RDU170320), and the support of Research Acculturation Collaborative Effort (RACE) RDU151314, Research Acculturation Grant Scheme (RAGS) RDU151404, provided by the Ministry of Higher Education, Malaysia. The project was also supported by Universiti Teknologi Malaysia (http://www.utm.my) UTM Research University Grant (RUG16H21).

References

[1] R. Asri, et al., A review of hydroxyapatite-based coating techniques: sol–gel and electrochemical depositions on biocompatible metals, J. Mech. Behav. Biomed. Mater. 57 (2016) 95–108.
[2] R. Asri, et al., Corrosion and surface modification on biocompatible metals: a review, Mater. Sci. Eng. C 77 (2017) 1261–1274.
[3] M. Hamidi, et al., A review of biocompatible metal injection moulding process parameters for biomedical applications, Mater. Sci. Eng. C 78 (2017) 1263–1276.
[4] W. Harun, et al., A comprehensive review of hydroxyapatite-based coatings adhesion on metallic biomaterials, Ceram. Int. 44 (2017) 1250–1268.
[5] H. Miura, Advanced powder processing techniques of Ti alloy powders for medical and aerospace applications, J. Korean Powder Metall. Inst. 20 (2013) 323–331.
[6] W. Harun, et al., A review of powder additive manufacturing processes for metallic biomaterials, Powder Technol. 327 (2017) 128–151.
[7] N. Manam, et al., Study of corrosion in biocompatible metals for implants: a review, J. Alloys Compd. 701 (2017) 698–715.
[8] C.M. Fernandes, A.M.R. Senos, M.T. Vieira, Particle surface properties of stainless steel-coated tungsten carbide powders, Powder Technol. 164 (2006) 124–129.
[9] I. Cristofolini, et al., Study of the uniaxial cold compaction of AISI 316L stainless steel powders through single action tests, Powder Technol. 295 (2016) 284–295.
[10] B. AlMangour, D. Grzesiak, J.-M. Yang, Selective laser melting of TiB 2/316L stainless steel composites: the roles of powder preparation and hot isostatic pressing post-treatment, Powder Technol. 309 (2017) 37–48.
[11] M. Aslam, et al., Powder injection molding of biocompatible stainless steel biodevices, Powder Technol. 295 (2016) 84–95.
[12] M. Belgacem, B. Thierry, G. Jean-Claude, Investigations on thermal debinding process for fine 316L stainless steel feedstocks and identification of kinetic parameters from coupling experiments and finite element simulations, Powder Technol. 235 (2013) 192–202.
[13] J.-P. Choi, et al., Investigation of the rheological behavior of 316L stainless steel micro-nano powder feedstock for micro powder injection molding, Powder Technol. 261 (2014) 201–209.
[14] C. Duan, et al., Nitriding of Fe–18Cr–8Mn stainless steel powders by mechanical alloying method with dual nitrogen source, Powder Technol. 294 (2016) 330–337.
[15] O. Ertugrul, et al., Effect of particle size and heating rate in microwave sintering of 316L stainless steel, Powder Technol. 253 (2014) 703–709.
[16] W.S.W. Harun, et al., Effect of MIM processing parameters on the properties of 440C stainless steel, J. Jpn. Soc. Powder Powder Metall. 59 (2012) 264–271.
[17] M. Javanbakht, E. Salahinejad, M. Hadianfard, The effect of sintering temperature on the structure and mechanical properties of medical-grade powder metallurgy stainless steels, Powder Technol. 289 (2016) 37–43.
[18] N. Kurgan, R. Varol, Mechanical properties of P/M 316L stainless steel materials, Powder Technol. 201 (2010) 242–247.
[19] A. Li, et al., Sintering diagram for 316L stainless steel fibers, Powder Technol. 288 (2016) 109–116.
[20] L. Liu, et al., Microstructure evolution of 316L stainless steel micro components prepared by micro powder injection molding, Powder Technol. 206 (2011) 246–251.
[21] B.N. Mukund, B. Hausnerova, T.S. Shivashankar, Development of 17-4PH stainless steel bimodal powder injection molding feedstock with the help of interparticle spacing/lubricating liquid concept, Powder Technol. 283 (2015) 24–31.
[22] J. Park, et al., Complex effects of alloy composition and porosity on the phase transformations and mechanical properties of powder metallurgy steels, Powder Technol. 284 (2015) 459–466.
[23] C. Quinard, T. Barriere, J.C. Gelin, Development and property identification of 316L stainless steel feedstock for PIM and μPIM, Powder Technol. 190 (2009) 123–128.
[24] C. Quinard, et al., Elaboration of PIM feedstocks with 316L fine stainless steel powders for the processing of micro-components, Powder Technol. 208 (2011) 383–389.
[25] M.R. Raza, et al., Effects of solid loading and cooling rate on the mechanical properties and corrosion behavior of powder injection molded 316 L stainless steel, Powder Technol. 289 (2016) 135–142.
[26] E. Salahinejad, R. Amini, M. Hadianfard, Structural evolution during mechanical alloying of stainless steels under nitrogen, Powder Technol. 215 (2012) 247–253.
[27] K.-H. Tseng, Development and application of oxide-based flux powder for tungsten inert gas welding of austenitic stainless steels, Powder Technol. 233 (2013) 72–79.
[28] J.-P. Choi, et al., Sintering behavior of 316L stainless steel micro–nanopowder compact fabricated by powder injection molding, Powder Technol. 279 (2015) 196–202.
[29] A. Fedorikova, et al., Mechanical properties of powder CoCrW-alloy prepared by am technology, MM Sci. J. (06) (2016) 1586–1589.
[30] C.G.S. Anwar, et al., Finite element analysis of porous medical grade cobalt chromium alloy structures produced by selective laser melting, Adv. Mater. Res. 1133 (2016).
[31] Z.A.M. Taib, et al., Dimensional accuracy study of open cellular structure CoCrMo alloy fabricated by selective laser melting process, Adv. Mater. Res. 1133 (2016) 280.
[32] J. Tong, et al., Fabrication of micro-fine spherical high Nb containing TiAl alloy powder based on reaction synthesis and RF plasma spheroidization, Powder Technol. 283 (2015) 9–15.
[33] L.E. Murr, et al., Microstructure and mechanical properties of open-cellular biomaterials prototypes for total knee replacement implants fabricated by electron beam melting, J. Mech. Behav. Biomed. Mater. 4 (2011) 1396–14411.
[34] J. Živčák, M. Šarik, R. Hudák, FEA simulation of thermal processes during the direct metal laser sintering of Ti64 titanium powder, Measurement 94 (2016) 893–901.
[35] E.T. Akinlabi, et al., Effect of scanning speed on material efficiency of laser metal deposited Ti6Al4V, World Acad. Sci. Eng. Technol. 71 (2012) 1531–1535.
[36] M.F. Erinosho, E.T. Akinlabi, S. Pityana, Laser metal deposition of Ti6Al4V/Cu composite: a study of the effect of laser power on the evolving properties, Proceedings of the World Congress on Engineering, 2, 2014, pp. 1205–1206.
[37] R.M. Mahamood, E.T. Akinlabi, Laser metal deposition of functionally graded Ti6Al4V/TiC, Mater. Des. 84 (2015) 402–410.

[38] R.M. Mahamood, E.T. Akinlabi, Effect of laser power and powder flow rate on the wear resistance behaviour of laser metal deposited TiC/Ti6Al4V composites, Mater. Today 2 (2015) 2679–2686.
[39] R.M. Mahamood, E.T. Akinlabi, Processing parameters optimization for material deposition efficiency in laser metal deposited titanium alloy, Lasers in Manuf. Mater. Process. 3 (2016) 9–21.
[40] R.M. Mahamood, et al., Effect of laser power on material efficiency, layer height and width of laser metal deposited Ti6Al4V, World Congress on Engineering and Computer Science (WCECS), 2, 2012, pp. 1–6.
[41] R.M. Mahamood, et al., Characterizing the effect of laser power density on microstructure, microhardness, and surface finish of laser deposited titanium alloy, J. Manuf. Sci. Eng. 135 (2013), 064502.
[42] R.M. Mahamood, et al., Laser metal deposition of Ti6Al4V: a study on the effect of laser power on microstructure and microhardness, International MultiConference of Engineers and Computer Scientists 2013, p. 2.
[43] R.M. Mahamood, et al., Material efficiency of laser metal deposited Ti6Al4V: effect of laser power, Int. Assoc. Eng. 21 (2013) 1–5.
[44] R.M. Mahamood, et al., Scanning velocity influence on microstructure, microhardness and wear resistance performance of laser deposited Ti6Al4V/TiC composite, Mater. Des. 50 (2013) 656–666.
[45] R.M. Mahamood, et al., Characterization of laser deposited Ti6Al4V/TiC composite powders on a Ti6Al4V substrate, Lasers Eng. 29 (2014) 197–213.
[46] R. Wauthle, et al., Effects of build orientation and heat treatment on the microstructure and mechanical properties of selective laser melted Ti6Al4V lattice structures, Addit. Manuf. 5 (2015) 77–84.
[47] R. Wauthle, et al., Revival of pure titanium for dynamically loaded porous implants using additive manufacturing, Mater. Sci. Eng. C 54 (2015) 94–100.
[48] F. Trevişan, et al., Additive manufacturing of titanium alloys in the biomedical field: processes, properties and applications, J. Appl. Biomater. Funct. Mater. 11 (2017) 1–6.
[49] B. Arifvianto, M. Leeflang, J. Zhou, The compression behaviors of titanium/carbamide powder mixtures in the preparation of biomedical titanium scaffolds with the space holder method, Powder Technol. 284 (2015) 112–121.
[50] V. Balaji, S. Kumaran, Densification and microstructural studies of titanium–boron carbide (B 4 C) powder mixture during spark plasma sintering, Powder Technol. 264 (2014) 536–540.
[51] A. Chen, et al., Enhanced sunlight photocatalytic activity of porous TiO 2 hierarchical nanosheets derived from petal template, Powder Technol. 249 (2013) 71–76.
[52] J.-W. Chen, et al., Hybrid metal oxides quantum dots/TiO 2 block composites: facile synthesis and photocatalysis application, Powder Technol. 246 (2013) 108–116.
[53] W. Chen, et al., Cold compaction study of Armstrong process® Ti–6Al–4V powders, Powder Technol. 214 (2011) 194–199.
[54] S. Chikosha, T. Shabalala, H. Chikwanda, Effect of particle morphology and size on roll compaction of Ti-based powders, Powder Technol. 264 (2014) 310–319.
[55] C.S.S. de Oliveira, et al., Study of the porous Ti35nb alloy processing parameters for implant applications, Powder Technol. 281 (2015) 91–98.
[56] V.Y. Filimonov, et al., High temperature synthesis of single-phase Ti 3 Al intermetallic compound in mechanically activated powder mixture, Powder Technol. 235 (2013) 606–613.
[57] S. Ghadikolaei, et al., Investigation on thermophysical properties of Tio2–Cu/H2O hybrid nanofluid transport dependent on shape factor in MHD stagnation point flow, Powder Technol. 322 (2017) 428–438.
[58] M.D. Hayat, et al., Modification of PEG/PMMA binder by PVP for titanium metal injection moulding, Powder Technol. 315 (2017) 243–249.
[59] D. Lin, et al., Rheological and thermal debinding properties of blended elemental Ti-6Al-4V powder injection molding feedstock, Powder Technol. 311 (2017) 357–363.
[60] X. Lu, et al., Influence of process parameters on the characteristics of TiAl alloyed powders by fluidized bed jet milling, Powder Technol. 254 (2014) 235–240.
[61] A. Manonukul, et al., Rheological properties of commercially pure titanium slurry for metallic foam production using replica impregnation method, Powder Technol. 266 (2014) 129–134.
[62] Y. Miao, et al., Facile and new synthesis of cobalt doped mesoporous TiO 2 with high visible-light performance, Powder Technol. 266 (2014) 365–371.
[63] B. Milicevic, M. Marinovic-Cincovic, M.D. Dramicanin, Non-isothermal crystallization kinetics of Y (2) Ti (2) O7, Powder Technol. 310 (2017) 67–73.
[64] S. Mohapatra, D.K. Mishra, S.K. Singh, Microscopic and spectroscopic analyses of TiC powder synthesized by thermal plasma technique, Powder Technol. 237 (2013) 41–45.
[65] H. Nersisyan, et al., Effective two-step method for producing Ti–6Al–4V alloy particles with various morphologies, Powder Technol. 254 (2014) 57–62.
[66] K. Ohenoja, M. Illikainen, J. Niinimäki, Effect of operational parameters and stress energies on the particle size distribution of TiO 2 pigment in stirred media milling, Powder Technol. 234 (2013) 91–96.
[67] J.-J. Park, et al., Effects of metal additions on refinement behavior of TiC particles during a very high speed milling process, Powder Technol. 249 (2013) 126–133.
[68] K.-M. Roh, et al., Comparison of deoxidation capability for preparation of low oxygen content powder from TiNi alloy scraps, Powder Technol. 253 (2014) 266–269.
[69] F. Saba, et al., Preparing TiC coating on AISI D2 steel using mechanical milling technique, Powder Technol. 246 (2013) 229–234.
[70] M. Sadeghalvaad, S. Sabbaghi, The effect of the TiO 2/polyacrylamide nanocomposite on water-based drilling fluid properties, Powder Technol. 272 (2015) 113–119.
[71] H. Salimi-Yasar, et al., Experimental investigation of thermal properties of cutting fluid using soluble oil-based TiO 2 nanofluid, Powder Technol. 310 (2017) 213–220.
[72] R. Schmidt, et al., Powder metallurgical processing of low modulus β-type Ti-45Nb to bulk and macro-porous compacts, Powder Technol. 322 (2017) 393–401.
[73] Q. Sun, et al., Influence of calcination temperature on the structural, adsorption and photocatalytic properties of TiO 2 nanoparticles supported on natural zeolite, Powder Technol. 274 (2015) 88–97.
[74] G. Thavanayagam, et al., Analysis of rheological behaviour of titanium feedstocks formulated with a water-soluble binder system for powder injection moulding, Powder Technol. 269 (2015) 227–232.
[75] H. Wang, et al., Characterization of the structure of TiB2/TiC composites prepared via mechanical alloying and subsequent pressureless sintering, Powder Technol. 217 (2012) 340–346.
[76] S. Wang, et al., Effect of mechanical alloying on the microstructure and properties of W–Ti alloys fabricated by spark plasma sintering, Powder Technol. 302 (2016) 1–7.
[77] S. Wang, et al., Microstructure and properties of TiN-reinforced W–Ti alloys prepared by spark plasma sintering, Powder Technol. 294 (2016) 301–306.
[78] Z. Yan, et al., Preparation and properties of Ti–4.5 Al–6.8 Mo–1.5 Fe alloy by high-velocity compaction, Powder Technol. 246 (2013) 345–350.
[79] Y. Yang, D. Mu, Rapid dehydrogenation of TiH 2 and its effect on formation mechanism of TiC during self-propagation high-temperature synthesis from TiH 2–C system, Powder Technol. 249 (2013) 208–211.
[80] C.-T. Yu, W.-C. Chen, Preparation, characterization of Ca/Al carbonate pellets with TiO 2 binder and CO 2 sorption at elevated-temperature conditions, Powder Technol. 239 (2013) 492–498.
[81] X. Zhao, et al., Preparation of nanosized anatase TiO 2-coated illite composite pigments by Ti (SO 4) 2 hydrolysis, Powder Technol. 271 (2015) 262–269.
[82] H. Zhu, et al., Reaction mechanisms of the TiC/Fe composite fabricated by exothermic dispersion from Fe–Ti–C element system, Powder Technol. 246 (2013) 456–461.
[83] M.D. Hayat, et al., Effect of PEG molecular weight on rheological properties of Ti-MIM feedstocks and water debinding behaviour, Powder Technol. 270 (2015) 296–301.
[84] Y. Wang, et al., Development of highly porous titanium scaffolds by selective laser melting, Mater. Lett. 64 (2010) 674–676.
[85] X.-b. SU, et al., Development of porous medical implant scaffolds via laser additive manufacturing, Trans. Nonferrous Metals Soc. China 22 (2012) s181–s187.
[86] S. Van Bael, et al., The effect of pore geometry on the in vitro biological behavior of human periosteum-derived cells seeded on selective laser-melted Ti6Al4V bone scaffolds, Acta Biomater. 8 (2012) 2824–2834.
[87] X. Wang, et al., Topological design and additive manufacturing of porous metals for bone scaffolds and orthopaedic implants: a review, Biomaterials 83 (2016) 127–141.
[88] X. Ren, et al., 3D gel-printing—an additive manufacturing method for producing complex shape parts, Mater. Des. 101 (2016) 80–87.
[89] A.M. Aboutaleb, et al., Accelerated process optimization for laser-based additive manufacturing by leveraging similar prior studies, IISE Trans. 49 (2017) 31–44.
[90] D. Bourell, et al., Materials for additive manufacturing, CIRP Ann. 66 (2017) 659–681.
[91] P. Petrousek, et al., Mechanical properties and porosity of Ti-6Al-4V alloy prepared by AM technology, MM Sci. J. 1 (2017) 1752–1755.
[92] S.M. Yusuf, N. Gao, Influence of energy density on metallurgy and properties in metal additive manufacturing, Mater. Sci. Technol. 33 (2017) 1269–1289.
[93] L. Fedorová, et al., A comparison of mechanical properties of lumbar bilateral implants manufactured by additive and conventional technologies, Key Eng. Mater. 635 (2015) 139–142.
[94] R. Wauthle, et al., Additively manufactured porous tantalum implants, Acta Biomater. 14 (2015) 217–225.
[95] A. Strondl, et al., Characterization and control of powder properties for additive manufacturing, JOM 67 (2015) 549–554.
[96] T. Toth, R. Hudak, J. Zivcak, Dimensional verification and quality control of implants produced by, Addit. Manuf. 19 (2015) 9.
[97] H. Mazhar, T. Osswald, D. Negrut, On the use of computational multi-body dynamics analysis in SLS-based 3D printing, Addit. Manuf. 12 (Part B) (2016) 291–295.
[98] S. Amin Yavari, et al., Effects of bio-functionalizing surface treatments on the mechanical behavior of open porous titanium biomaterials, J. Mech. Behav. Biomed. Mater. 36 (2014) 109–119.
[99] S.A. Yavari, et al., Crystal structure and nanotopographical features on the surface of heat-treated and anodized porous titanium biomaterials produced using selective laser melting, Appl. Surf. Sci. 290 (2014) 287–294.
[100] S. Zhang, et al., Effects of scan line spacing on pore characteristics and mechanical properties of porous Ti6Al4V implants fabricated by selective laser melting, Mater. Des. 63 (2014) 185–193.
[101] T. Bormann, et al., Microstructure of selective laser melted nickel–titanium, Mater. Charact. 94 (2014) 189–202.
[102] J. Vaithilingam, et al., Functionalisation of Ti6Al4V components fabricated using selective laser melting with a bioactive compound, Mater. Sci. Eng. C 46 (2015) 52–61.
[103] G. Rolink, et al., Laser metal deposition and selective laser melting of Fe–28 at.% Al, J. Mater. Res. 29 (2014) 2036–2043.
[104] F. Trevisan, et al., On the selective laser melting (SLM) of the AlSi10Mg alloy: process, microstructure, and mechanical properties, Materials 10 (2017) 76.
[105] G. Yablokova, et al., Rheological behavior of β-Ti and NiTi powders produced by atomization for SLM production of open porous orthopedic implants, Powder Technol. 283 (2015) 199–209.
[106] S.A. Yavari, et al., Fatigue behavior of porous biomaterials manufactured using selective laser melting, Mater. Sci. Eng. C 33 (2013) 4849–4858.
[107] A. Aversa, et al., A study of the microstructure and the mechanical properties of an Al Si Ni alloy produced via selective laser melting, J. Alloys Compd. 695 (2017) 1470–1478.

[108] J.-P. Choi, et al., Densification and microstructural investigation of Inconel 718 parts fabricated by selective laser melting, Powder Technol. 310 (2017) 60–66.
[109] R. Li, et al., Selective laser melting of a novel Sc and Zr modified Al-6.2 Mg alloy: processing, microstructure, and properties, Powder Technol. 319 (2017) 117–128.
[110] F. Calignano, et al., Influence of process parameters on surface roughness of aluminum parts produced by DMLS, Int. J. Adv. Manuf. Technol. 67 (2013) 2743–2751.
[111] D. Manfredi, et al., Direct Metal Laser Sintering: an additive manufacturing technology ready to produce lightweight structural parts for robotic applications, La Metall. Ital. 1 (2013) 15–24.
[112] D. Manfredi, et al., From powders to dense metal parts: characterization of a commercial AlSiMg alloy processed through direct metal laser sintering, Materials 6 (2013) 856–869.
[113] M. Koike, et al., Evaluation of titanium alloy fabricated using electron beam melting system for dental applications, J. Mater. Process. Technol. 211 (2011) 1400–1408.
[114] H. Galarraga, et al., Effects of heat treatments on microstructure and properties of Ti-6Al-4V ELI alloy fabricated by electron beam melting (EBM), Mater. Sci. Eng. A 685 (2017) 417–428.
[115] W.Q. Toh, et al., Comparative study on tribological behavior of Ti-6Al-4V and Co-Cr-Mo samples additively manufactured with electron beam melting, Prog. Addit. Manuf. 1 (2016) 342–348.
[116] S. Zhao, et al., Microstructure and mechanical properties of open cellular Ti-6Al-4V prototypes fabricated by electron beam melting for biomedical applications, Mater. Technol. 31 (2016) 98–107.
[117] X. Zhao, et al., Comparison of the microstructures and mechanical properties of Ti-6Al-4V fabricated by selective laser melting and electron beam melting, Mater. Des. 95 (2016) 21–31.
[118] A. Hinojos, et al., Joining of Inconel 718 and 316 Stainless Steel using electron beam melting additive manufacturing technology, Mater. Des. 94 (2016) 17–27.
[119] L.E. Murr, et al., Metal fabrication by additive manufacturing using laser and electron beam melting technologies, J. Mater. Sci. Technol. 28 (2012) 1–14.
[120] M. Terner, et al., Electron beam melting of high niobium containing TiAl alloy: feasibility investigation, Steel Res. Int. 83 (2012) 943–949.
[121] S. Biamino, et al., Electron beam melting of Ti–48Al–2Cr–2Nb alloy: microstructure and mechanical properties investigation, Intermetallics 19 (2011) 776–781.
[122] A. Bandyopadhyay, et al., Influence of porosity on mechanical properties and in vivo response of Ti6Al4V implants, Acta Biomater. 6 (2010) 1640–1648.
[123] F.A. España, et al., Design and fabrication of CoCrMo alloy based novel structures for load bearing implants using laser engineered net shaping, Mater. Sci. Eng. C 30 (2010) 50–57.
[124] M.S. Hossain, et al., Fabrication of smart parts using powder bed fusion additive manufacturing technology, Addit. Manuf. 10 (2016) 58–66.
[125] E. Börjesson, et al., Evaluation of particle measures relevant for powder bed porosity—a study of spray dried dairy powders, Powder Technol. 253 (2014) 453–463.
[126] S.L. Sing, et al., Laser and electron-beam powder-bed additive manufacturing of metallic implants: a review on processes, materials and designs, J. Orthop. Res. 34 (2016) 369–385.
[127] A.T. Sutton, et al., Powders for additive manufacturing processes: characterization techniques and effects on part properties, Solid Freeform Fabrication, 1, 2016, pp. 1004–1030.
[128] D. Hyndavi, S. Murthy, Rapid Prototyping Technology-Classification and Comparison, Int. Res. J. Eng. Technol. 4 (2017) 3107–3111.
[129] M. Cima, et al., Three-dimensional printing techniques, Google Patents, 1995.
[130] A.J. Dunbar, et al., Comparisons of laser powder bed fusion additive manufacturing builds through experimental in situ distortion and temperature measurements, Addit. Manuf. 15 (2017) 57–65.
[131] T. Wohlers, T. Gornet, History of additive manufacturing, Wohlers Report: Additive Manufacturing and 3D Printing State of the Industry Annual Worldwide Progress Report, 2011.
[132] W.J. Sames, et al., The metallurgy and processing science of metal additive manufacturing, Int. Mater. Rev. 61 (2016) 315–360.
[133] D. White, Ultrasonic object consolidation, Google Patents., 2003.
[134] D. White, D.E. Carmein, Ultrasonic object consolidation system and method, Google Patents, 2002.
[135] W. Sames, Additive Manufacturing of Inconel 718 Using Electron Beam Melting: Processing, Post-processing, & Mechanical Properties, 2015.
[136] R. Larson, Method and device for producing three-dimensional bodies, Google Patents1998.
[137] M. Molitch-Hou, Desktop Metal's CTO on the Next Generation of Metal 3D Printing, 2017.
[138] M. Shellabear, O. Nyrhilä, DMLS-development history and state of the art, Laser Assist. Netshape Eng. 4 (4) (2004) 21–24.
[139] A. Bandyopadhyay, H. Sahasrabudhe, S. Bose, 6 - Laser surface modification of metallic biomaterials A2 - Vilar, Rui, in Laser Surface Modification of Biomaterials, Woodhead Publishing, 2016 175–195.
[140] S. Magnus, Additive manufacturing-a revolution in progress? An overview, Int. J. Adv. Manuf. Technol. 1 (2018) 1–15.
[141] M. Yan, P. Yu, An Overview of Densification, Microstructure and Mechanical Property of Additively Manufactured Ti-6Al-4V—Comparison among Selective Laser Melting, Electron Beam Melting, Laser Metal Deposition and Selective Laser Sintering, and with Conventional Powder, Sintering Techniques of Materials, InTech, 2015.
[142] D. Gu, Laser additive manufacturing (am): classification, processing philosophy, and metallurgical mechanisms, Laser Additive Manufacturing of High-Performance Materials, Springer 2015, pp. 15–71.
[143] C.R. Deckard, Method for producing parts by selective sintering, Google Patents, 1997.
[144] L.E. Murr, et al., Fabrication of metal and alloy components by additive manufacturing: examples of 3D materials science, J. Mater. Res. Technol. 1 (2012) 42–54.
[145] L. Murr, et al., Microstructure and mechanical behavior of Ti–6Al–4V produced by rapid-layer manufacturing, for biomedical applications, J. Mech. Behav. Biomed. Mater. 2 (2009) 20–32.
[146] P. Petroušek, et al., Mechanical properties and porosity of Ti-6Al-4V alloy prepared by AM technology, 1 (2017) 1752–1755.
[147] H. Hack, et al., Mechanical properties of additive manufactured nickel alloy 625, Addit. Manuf. 14 (2017) 105–115.
[148] A. Mazzoli, et al., Selective laser sintering manufacturing of polycaprolactone bone scaffolds for applications in bone tissue engineering, Rapid Prototyp. J. 21 (2015) 386–392.
[149] F.-H. Liu, et al., Selective laser sintering of bio-metal scaffold, Procedia CIRP 5 (2013) 83–87.
[150] A. Lou, C. Grosvenor, Selective Laser Sintering, Birth of an Industry, 2012.
[151] S. Kirboga, M. Öner, Application of experimental design for the precipitation of calcium carbonate in the presence of biopolymer, Powder Technol. 249 (2013) 95–104.
[152] M. Van den Eynde, L. Verbelen, P. Van Puyvelde, Assessing polymer powder flow for the application of laser sintering, Powder Technol. 286 (2015) 151–155.
[153] J. Maszybrocka, A. Stwora, B. Gapinski, G. Skrabalak, M. Karolus, Morphology and surface topography of Ti6Al4V lattice structure fabricated by selective laser sintering, Bull. Pol. Acad. Sci. Tech. Sci. 65 (2017) 85–92.
[154] C. Yan, et al., Ti–6Al–4V triply periodic minimal surface structures for bone implants fabricated via selective laser melting, J. Mech. Behav. Biomed. Mater. 5 (2015) 61–73.
[155] S. Van Bael, et al., Micro-CT-based improvement of geometrical and mechanical controllability of selective laser melted Ti6Al4V porous structures, Mater. Sci. Eng. A 528 (2011) 7423–7431.
[156] A. Cheng, et al., Laser sintered porous Ti–6Al–4V implants stimulate vertical bone growth, Ann. Biomed. Eng. 45 (2017) 1–11.
[157] A. Cheng, et al., Laser sintered constructs with bio-inspired porosity and surface micro/nano roughness enhance mesenchymal stem cell differentiation and matrix mineralization in vitro, Tissue Int. 99 (2016) 625–637.
[158] S. Hyzy, et al., Novel hydrophilic nanostructured microtexture on direct metal laser sintered Ti-6Al-4V surfaces enhances osteoblast response in vitro and osseointegration in a rabbit model, J. Biomed. Mater. Res. A 104 (2016) 2086–2098.
[159] M. Ahmed, et al., The effect of thermo-mechanical processing and ageing time on microstructure and mechanical properties of powder metallurgy near β titanium alloys, J. Alloys Compd. 714 (2017) 610–618.
[160] D. Greitemeier, et al., Fatigue performance of additive manufactured TiAl6V4 using electron and laser beam melting, Int. J. Fatigue 94 (2017) 211–217.
[161] A. Bandyopadhyay, et al., In vivo response of laser processed porous titanium implants for load-bearing implants, Ann. Biomed. Eng. 45 (2017) 249–260.
[162] M.P. Echlin, et al., Incipient slip and long range plastic strain localization in microtextured Ti-6Al-4V titanium, Acta Mater. 114 (2016) 164–175.
[163] S. Balachandran, S. Kumar, D. Banerjee, On recrystallization of the α and β phases in titanium alloys, Acta Mater. 131 (2017) 423–434.
[164] S. Ghani, et al., Dimensional accuracy of internal cooling channel made by selective laser melting (SLM) and direct metal laser sintering (DMLS) processes in fabrication of internally cooled cutting tools, MATEC Web Conf. 90 (2017), 01058.
[165] F. Calignano, et al., Direct fabrication of joints based on direct metal laser sintering in aluminum and titanium alloys, Procedia CIRP 21 (2014) 129–132.
[166] A. Bača, et al., Influence of build direction on the fatigue behaviour of Ti6Al4V alloy produced by direct metal laser sintering, Mater. Today 3 (2016) 921–924.
[167] J. Brezinová, et al., Direct metal laser sintering of Ti6Al4V for biomedical applications: microstructure, Corros. Prop. Mech. Treat. Implants 6 (2016) 171.
[168] A. Guzanová, et al., Influence of build orientation, heat treatment, and laser power on the hardness of Ti6Al4V manufactured using the DMLS process, Metals 7 (2017) 318.
[169] W. Harun, S. Safian, M. Idris, Evaluation of ABS patterns produced from FDM for investment casting process, Computational Method and Experiments in Materials Characterisation IV, 64, 2009, pp. 319–328.
[170] S.H. Ahmed, et al., Effect of process parameters on hardness, temperature profile and solidification of different layers processed by direct metal laser sintering (*DMLS*), AIP Conference Proceedings, AIP Publishing, 2016.
[171] Y. Xu, et al., Effect of annealing treatments on the microstructure, mechanical properties and corrosion behavior of direct metal laser sintered Ti-6Al-4V, J. Mater. Eng. Perform. 26 (2017) 2572–2582.
[172] R. Konečná, et al., High cycle fatigue life of Ti6Al4V alloy produced by direct metal laser sintering, Solid State Phenom. 258 (2017) 522–525.
[173] S. Wu, et al., Microstructural evolution and microhardness of a selective-laser-melted Ti–6Al–4V alloy after post heat treatments, J. Alloys Compd. 672 (2016) 643–652.
[174] A. Bača, R. Konečná, G. Nicoletto, Influence of the direct metal laser sintering process on the fatigue behavior of the Ti6Al4V alloy, Mater. Sci. Forum 891 (2017) 317–321.
[175] T.M. Mower, M.J. Long, Mechanical behavior of additive manufactured, powder-bed laser-fused materials, Mater. Sci. Eng. A 651 (2016) 198–213.
[176] B. Vrancken, et al., Heat treatment of Ti6Al4V produced by selective laser melting: microstructure and mechanical properties, J. Alloys Compd. 541 (2012) 177–185.
[177] D.A. Hollander, et al., Structural, mechanical and in vitro characterization of individually structured Ti–6Al–4V produced by direct laser forming, Biomaterials 27 (2006) 955–963.
[178] B. Ellyson, M. Brochu, M. Brochu, Characterization of bending vibration fatigue of SLM fabricated Ti-6Al-4V, Int. J. Fatigue 99 (2017) 25–34.

[179] B. Van Hooreweder, et al., Improving the fatigue performance of porous metallic biomaterials produced by selective laser melting, Acta Biomater. 47 (2017) 193–202.
[180] B. Van Hooreweder, J.-P. Kruth, Advanced fatigue analysis of metal lattice structures produced by selective laser melting, CIRP Ann. Manuf. Technol. 66 (2017) 221–224.
[181] B. Van Hooreweder, et al., Analysis of fracture toughness and crack propagation of Ti6Al4V produced by selective laser melting, Adv. Eng. Mater. 14 (2012) 92–97.
[182] Y. Shen, D. Gu, P. Wu, Development of porous 316L stainless steel with controllable microcellular features using selective laser melting, Mater. Sci. Technol. 24 (2008) 1501–1505.
[183] C.F.W. Lindemann, U. Jahnke, 11 - Modelling of laser additive manufactured product lifecycle costs A2 - Brandt, Milan, Laser Additive Manufacturing, Woodhead Publishing, Cambridge 2017, pp. 281–316.
[184] S. Dadbakhsh, et al., Effect of SLM parameters on transformation temperatures of shape memory nickel titanium parts, Adv. Eng. Mater. 16 (2014) 1140–1146.
[185] X. Li, J. Van Humbeeck, J.-P. Kruth, Selective laser melting of weak-textured commercially pure titanium with high strength and ductility: a study from laser power perspective, Mater. Des. 116 (2017) 352–358.
[186] L. Thijs, et al., A study of the microstructural evolution during selective laser melting of Ti–6Al–4V, Acta Mater. 58 (2010) 3303–3312.
[187] B. Vrancken, et al., Microstructure and mechanical properties of a novel β titanium metallic composite by selective laser melting, Acta Mater. 68 (2014) 150–158.
[188] N. Poondla, et al., A study of the microstructure and hardness of two titanium alloys: commercially pure and Ti–6Al–4V, J. Alloys Compd. 486 (2009) 162–167.
[189] S.-D. Sun, et al., Hot deformation behavior and microstructure evolution of TC4 titanium alloy, Trans. Nonferrous Metals Soc. China 20 (2010) 2181–2184.
[190] J. Sun, Y. Yang, D. Wang, Mechanical properties of a Ti6Al4V porous structure produced by selective laser melting, Mater. Des. 49 (2013) 545–552.
[191] S.-c Liao, J. Duffy, Adiabatic shear bands in a Ti-6Al-4V titanium alloy, J. Mech. Phys. Solids 46 (1998) 2201–2231.
[192] N. Biswas, et al., Deformation and fracture behavior of laser processed dense and porous Ti6Al4V alloy under static and dynamic loading, Mater. Sci. Eng. A 549 (2012) 213–221.
[193] L. Mullen, et al., Selective laser melting: a unit cell approach for the manufacture of porous, titanium, bone in-growth constructs, suitable for orthopedic applications. II. Randomized structures, J. Biomed. Mater. Res. B Appl. Biomater. 92 (2010) 178–188.
[194] L. Mullen, et al., Selective laser melting: a regular unit cell approach for the manufacture of porous, titanium, bone in-growth constructs, suitable for orthopedic applications, J. Biomed. Mater. Res. B Appl. Biomater. 89 (2009) 325–334.
[195] R. Stamp, et al., The development of a scanning strategy for the manufacture of porous biomaterials by selective laser melting, J. Mater. Sci. Mater. Med. 20 (2009) 1839–1848.
[196] T. Douglas, et al., Rapid prototyping: porous titanium alloy scaffolds produced by selective laser melting (SLM) for bone tissue engineering, Tissue Eng. A 15 (2009) 07–08.
[197] P.H. Warnke, et al., Rapid prototyping: porous titanium alloy scaffolds produced by selective laser melting for bone tissue engineering, Tissue Eng. Part C Methods 15 (2008) 115–124.
[198] I. Yadroitsev, P. Krakhmalev, I. Yadroitsava, Selective laser melting of Ti6Al4V alloy for biomedical applications: temperature monitoring and microstructural evolution, J. Alloys Compd. 583 (2014) 404–409.
[199] I. Yadroitsev, P. Bertrand, I. Smurov, Parametric analysis of the selective laser melting process, Appl. Surf. Sci. 253 (19) (2007) 8064–8069.
[200] M. Benedetti, et al., The effect of post-sintering treatments on the fatigue and biological behavior of Ti-6Al-4V ELI parts made by selective laser melting, J. Mech. Behav. Biomed. Mater. 71 (2017) 295–306.
[201] Lawrence E. Murr, et al., Next Generation Orthopaedic Implants by Additive manufacturing Using Electron Beammelting, 2012 1–14.
[202] X.Y. Cheng, et al., Compression deformation behavior of Ti-6Al-4V alloy with cellular structures fabricated by electron beam melting, J. Mech. Behav. Biomed. Mater. 16 (1) (2012) 153–162.
[203] S. Biamino, et al., Electron beam melting of Ti–48Al–2Cr–2Nb alloy: microstructure and mechanical properties investigation, Intermetallics 19 (6) (2011) 776–781.
[204] M. Sanna Fager Franzen, et al., Improved Resolution and Mechanical Properties of Porous Coatings and Cellular Structures In Ti6Al4V Manufactured with Electron Beam Melting, 2011.
[205] M. Mattias Svensson, et al., Improved Resolution of Porous, Lightweight Structures in Ti6Al4V Direct Manufactured with Electron Beam Melting, 2011.
[206] S.F. Franzén, et al., Influence of powder size and layer thickness on the properties of Ti-6Al-4V lattice structures manufactured by electron beam melting, 2 (2011).
[207] J. Karlsson, et al., Surface oxidation behavior of Ti–6Al–4V manufactured by Electron Beam Melting (EBM®), J. Manuf. Process. 17 (2015) 120–126.
[208] O.L. Harrysson, et al., Direct metal fabrication of titanium implants with tailored materials and mechanical properties using electron beam melting technology, Mater. Sci. Eng. C 28 (3) (2008) 366–373.
[209] G. Chahine, et al., The design and production of Ti-6Al-4V ELI customized dental implants, JOM 60 (11) (2008) 50–55.
[210] X. Li, et al., Fabrication and characterization of porous Ti6Al4V parts for biomedical applications using electron beam melting process, Mater. Lett. 63 (3–4) (2009) 403–405.
[211] P. Thomsen, et al., Electron beam-melted, free-form-fabricated titanium alloy implants: material surface characterization and early bone response in rabbits, J. Biomed. Mater. Res. B Appl. Biomater. 90 (1) (2009) 35–44.
[212] S. Ponader, et al., In vivo performance of selective electron beam-melted Ti-6Al-4V structures, J. Biomed. Mater. Res. A 92((1) (2010) 56–62.
[213] N. Khouja, et al., In vivo evaluation of novel custom. made press-fit implants, J. Dent. Res. 89 (2010) 1662.
[214] N. Khouja, et al., In vivo evaluation of novel experimental implants, J. Dent. Res. 89 (Spec Iss A) (2010) 1103.
[215] C.M. Haslauer, et al., In vitro biocompatibility of titanium alloy discs made using direct metal fabrication, Med. Eng. Phys. 32 (6) (2010) 645–652.
[216] M. Larsson, U. Lindhe, O. Harrysson, Rapid manufacturing with electron beam melting (EBM)—a manufacturing revolution? Solid Freeform Fabrication Symposium, Austin, TX, August, 2003.
[217] A. Christensen, R. Kircher, A. Lippincott, Qualification of electron beam melted (EBM) Ti6Al4V-ELI for orthopaedic applications, Medical Device Materials IV: Proceedings of the Materials and Processes for Medical Devices Conference, 2008.
[218] L. Murr, et al., Microstructure and mechanical behavior of Ti–6Al–4V produced by rapid-layer manufacturing, for biomedical applications, J. Mech. Behav. Biomed. Mater. 2 (1) (2009) 20–32.
[219] L. Murr, et al., Characterization of Ti–6Al–4V open cellular foams fabricated by additive manufacturing using electron beam melting, Mater. Sci. Eng. A 527 (7) (2010) 1861–1868.
[220] G.F. Vander Voort, et al., ASM handbook, Metallography and microstructures, 9, p. 44073-0002.
[221] L.E. Murr, W.L. Johnson, 3D metal droplet printing development and advanced materials additive manufacturing, J. Mater. Res. Technol. 1 (2017) 77–89.
[222] M. Guo, X. Li, Development of porous Ti6Al4V/chitosan sponge composite scaffold for orthopedic applications, Mater. Sci. Eng. C 58 (2016) 1177–1181.
[223] B. Mueller, Additive manufacturing technologies-rapid prototyping to direct digital manufacturing, Assem. Autom. 32 (2012) 1–48.
[224] R. Mahamood, E. Akinlabi, Laser Metal Deposition of Ti6Al4V/TiC, Mater. Des. 84 (2016) 402–410.
[225] R. Mahamood, E. Akinlabi, Microstructure and mechanical behaviour of laser metal deposited titanium alloy, Lasers in Engineering, 35, Old City Publishing 2016, pp. 27–38.
[226] R.M. Mahamood, E.T. Akinlabi, Scanning speed and powder flow rate influence on the properties of laser metal deposition of titanium alloy, Int. J. Adv. Manuf. Technol. 91 (2017) 2419–2426.
[227] R.M. Mahamood, E.T. Akinlabi, Scanning speed influence on the microstructure and micro hardness properties of titanium alloy produced by laser metal deposition process, Mater. Today (4) (2017) 5206–5214.
[228] R.M. Mahamood, E.T. Akinlabi, M.G. Owolabi, Effect of laser power and powder flow rate on dilution rate and surface finish produced during laser metal deposition of Titanium alloy, Mechanical and Intelligent Manufacturing Technologies, 1, 2017, pp. 6–10.
[229] H.R. Sandgren, et al., Characterization of fatigue crack growth behavior in LENS fabricated Ti-6Al-4V using high-energy synchrotron x-ray microtomography, Addit. Manuf. 12 (Part A) (2016) 132–141.
[230] Y. Zhai, H. Galarraga, D.A. Lados, Microstructure, static properties, and fatigue crack growth mechanisms in Ti-6Al-4V fabricated by additive manufacturing: LENS and EBM, Eng. Fail. Anal. 69 (2016) 3–14.
[231] R.J. Hebert, Viewpoint: metallurgical aspects of powder bed metal additive manufacturing, J. Mater. Sci. 51 (3) (2016) 1165–1175.
[232] W.E. Frazier, Metal additive manufacturing: a review, J. Mater. Eng. Perform. 23 (6) (2014) 1917–1928.
[233] S. Haeri, Optimisation of blade type spreaders for powder bed preparation in Additive Manufacturing using DEM simulations, Powder Technol. 321 (2017) 94–104.
[234] E.J. Parteli, T. Pöschel, Particle-based simulation of powder application in additive manufacturing, Powder Technol. 288 (2016) 96–102.
[235] V. Urlea, V. Brailovski, Electropolishing and electropolishing-related allowances for powder bed selectively laser-melted Ti-6Al-4V alloy components, J. Mater. Process. Technol. 242 (2017) 1–11.
[236] S.M. Yusuf, N. Gao, Influence of energy density on metallurgy and properties in metal additive manufacturing, Mater. Sci. Technol. (2017) 1–21.
[237] W.J. Sames, et al., The metallurgy and processing science of metal additive manufacturing, Int. Mater. Rev. 61 (5) (2016) 315–360.
[238] N. Kumbhar, A. Mulay, Post processing methods used to improve surface finish of products which are manufactured by additive manufacturing technologies: a review, J. Inst. Eng. (India) C (2016) 1–7.
[239] A. Ebrahimi, M. Saffari, T. Langrish, Spray drying and post-processing production of highly-porous lactose particles using sugars as templating agents, Powder Technol. 283 (2015) 171–177.
[240] N. Guo, M.C. Leu, Additive manufacturing: technology, applications and research needs, Front. Mech. Eng. 8 (3) (2013) 215–243.
[241] F. Klocke, et al., Wire-based laser metal deposition for additive manufacturing of TiAl6V4: basic investigations of microstructure and mechanical properties from build-up parts, Proc. SPIE 10095 (2017) 11.
[242] F. Calignano, et al., Overview on additive manufacturing technologies, Proc. IEEE 105 (4) (2017) 593–612.
[243] A. Gasser, et al., Laser additive manufacturing, Laser Tech. J. 7 (2) (2010) 58–63.
[244] A. Cheng, et al., Laser sintered porous Ti–6Al–4V implants stimulate vertical bone growth, Ann. Biomed. Eng. (2017) 1–11.
[245] A. Bandyopadhyay, et al., In vivo response of laser processed porous titanium implants for load-bearing implants, Ann. Biomed. Eng. 45 (1) (2017) 249–260.
[246] K. Kardel, et al., Addit. Manuf. 14 (2017) 87–94.
[247] D. Herzog, et al., Additive manufacturing of metals, Acta Mater. 117 (2016) 371–392.
[248] A. Chang, A Comprehensive Study on Additive Manufacturing and Machining, 2017.
[249] A. Chiappone, et al., Study of graphene oxide-based 3D printable composites: effect of the in situ reduction, Compos. Part B 124 (2017) 9–15.

[250] R. Amrousse, Deposition of activated alumina powder on SiC diesel particulate filters with wall flow type through in-situ hydrothermal process, Powder Technol. 286 (2015) 557–560.
[251] C. Cao, et al., In situ preparation of magnetic Fe 3 O 4/chitosan nanoparticles via a novel reduction–precipitation method and their application in adsorption of reactive azo dye, Powder Technol. 260 (2014) 90–97.
[252] S. Dehghanpour, et al., Cu 2 O microsphere, microspherical composite of Cu 2 O/Cu nanocrystals and various Cu microcrystals: in situ hydrothermal conversion of Cu-aminodiphosphonate complexes, Powder Technol. 246 (2013) 148–156.
[253] H.J. Prado, P.R. Bonelli, A.L. Cukierman, In situ fluidized hot melt granulation using a novel meltable binder: effect of formulation variables on granule characteristics and controlled release tablets, Powder Technol. 264 (2014) 498–506.
[254] Z. Yan, et al., Microstructure and mechanical properties of in-situ synthesized TiB whiskers reinforced titanium matrix composites by high-velocity compaction, Powder Technol. 267 (2014) 309–314.
[255] Z. Yu, et al., Processing and characterization of in-situ ultrafine TiB2-Cu composites from Ti-B-Cu system, Powder Technol. 320 (2017) 66–72.
[256] D.L. Cohen, et al., Additive manufacturing for in situ repair of osteochondral defects, Biofabrication 2 (3) (2010), 035004.
[257] X. Cui, et al., Cell damage evaluation of thermal inkjet printed Chinese hamster ovary cells, Biotechnol. Bioeng. 106 (6) (2010) 963–969.
[258] R. Whitwam, Startup Aims to Make 3D Metal Printing 100 Times Faster, 2017.
[259] L. Blain, 100× Faster, 10× Cheaper: 3D Metal Printing Is about to Go Mainstream, 2017.
[260] D. Rotman, The 3-D Printer that could Finally Change Manufacturing, 2017.
[261] W.S.W. Harun, et al., A review of powder additive manufacturing processes for metallic biomaterials, Powder Technol. 327 (2018) 128–151.